The Global Structure of UTLS Ozone in GEOS-5: A Multi-Year Assimilation of EOS Aura Data

Krzysztof Wargan[1,2], Steven Pawson[1], Mark A. Olsen[3,4], Jacquelyn C. Witte[2,3],

Anne R. Douglass[3], Jerald R. Ziemke[3,4], Susan E. Strahan[3,5], J. Eric Nielsen[1,2]

[1] Global Modeling and Assimilation Office, Code 610.1, NASA Goddard Space Flight
   Center, Greenbelt, MD

[2] Science Systems and Applications Inc., Lanham, MD

[3] Atmospheric Chemistry and Dynamics Laboratory, Code 614, NASA Goddard Space
   Flight Center, Greenbelt, MD

[4] Goddard Earth Sciences, Technology and Research Center, Morgan State University,
   Baltimore, MD.

[5] Goddard Earth Sciences, Technology and Research Center, Universities Space
   Research Association, Columbia, MD

Correspondence: Krzysztof.Wargan-1@nasa.gov

23   **Abstract**

24

25   Eight years of ozone measurements retrieved from the Ozone Monitoring Instrument

26   (OMI) and the Microwave Limb Sounder, both on the EOS Aura satellite, have been

27   assimilated into the Goddard Earth Observing System version 5 (GEOS-5) data

28   assimilation system. This study thoroughly evaluates this assimilated product,

29   highlighting its potential for science. The impact of observations on the GEOS-5 system

30   is explored by examining the spatial distribution of the observation-minus-forecast

31   statistics. Independent data are used for product validation. The correlation coefficient of

32   the lower-stratospheric ozone column with ozonesondes is 0.99 and the bias is 0.5%,

33   indicating the success of the assimilation in reproducing the ozone variability in that

34   layer. The upper-tropospheric assimilated ozone column is about 10% lower than the

35   ozonesonde column but the correlation is still high (0.87). The assimilation is shown to

36   realistically capture the sharp cross-tropopause gradient in ozone mixing ratio.

37   Occurrence of transport-driven low ozone laminae in the assimilation system is similar to

38   that obtained from the High Resolution Dynamics Limb Sounder (HIRDLS) above the

39   400 K potential temperature surface but the assimilation produces fewer laminae than

40   seen by HIRDLS below that surface. Although the assimilation produces 5 – 8 fewer

41   occurrences per day (up to ~20%) during the three years of HIRDLS data, the interannual

42   variability is captured correctly. This data-driven assimilated product is complementary

43   to ozone fields generated from chemistry and transport models. Applications include

44   study of the radiative forcing by ozone and tracer transport near the tropopause.

45

1. Introduction

This work describes and evaluates an eight-year long record of six-hourly global maps of ozone produced by NASA's Goddard Earth Observing System Version 5 (GEOS-5) data assimilation system informed by total ozone observations from the Ozone Monitoring Instrument (OMI) and stratospheric profile data provided by the Microwave Limb Sounder (MLS). Both instruments fly on the Earth Observing System Aura satellite (EOS Aura, launched in July 2004) and are still operational. In the past, several techniques were developed to produce global maps of tropospheric ozone columns using combined information from these two data sources. *Schoeberl et al.* [2007] employed a trajectory method to propagate MLS observations and calculate the stratospheric ozone columns. These were subsequently subtracted from the OMI total column measurements to obtain the tropospheric ozone residual. *Ziemke et al.* [2011] used MLS observations binned into a latitude-longitude grid collocated with gridded OMI data to generate a six-year global climatology of stratospheric and tropospheric ozone columns. *Stajner et al.* [2008] and *Wargan et al.* [2010] assimilated OMI and MLS data into the GEOS-4 data assimilation system (a predecessor of GEOS-5). Their work demonstrated good agreement of the assimilated product on synoptic time scales with independent observations in upper troposphere – lower stratosphere (UTLS), in particular, as compared to data from aircraft measurements.

The present work aims to investigate the realism of ozone structures in the UTLS in an assimilation of MLS and OMI observations from 2005 to 2012. The assimilation is performed using Version 5.7.2 of the GEOS-5 data assimilation system. While this study

69 focuses on the region between 500 hPa and 50 hPa, *Ziemke et al.* [2014] conducted a

70 detailed evaluation of the tropospheric ozone from this analysis with two other products

71 derived from OMI and MLS data (a tropospheric residual method and ozone profiles

72 retrieved from OMI-measured radiances). That work also includes an extensive

73 comparison of these three products with the Global Modeling Initiative chemical

74 transport model [*Duncan et al.*, 2008; *Strahan et al.*, 2007], which simulates global ozone

75 fields using a photochemical mechanism and transport driven by GEOS-5 meteorological

76 analysis but does not utilize any ozone data.

77 The production of global, three-dimensional ozone distributions derived from

78 observations, that resolve the ozone structure in the vicinity of the tropopause is

79 motivated by the importance of the ozone distribution to both climate forcing and

80 transport processes. Ozone in the UTLS plays an important role in the forcing of climate

81 and also impacts background tropospheric ozone levels that influence regional air quality.

82 The vertical distribution of ozone in the stratosphere and troposphere is important for

83 climate forcing, largely because of the dominant warming impact of tropospheric ozone,

84 which is partly offset by a weaker cooling impact of stratospheric ozone [e.g., *Lacis et*

85 *al.*, 1990]. Radiative cooling by water vapor and warming by ozone have been proposed

86 as a possible explanation for the existence and maintenance of the tropopause inversion

87 layer in the lowermost extratropical stratosphere [*Randel et al.*, 2007]. The sensitivity of

88 the outgoing long wave radiation to the ozone distribution was emphasized by a study of

89 radiative fluxes from the Tropospheric Emission Sounder (TES) by *Worden et al.* [2011].

90 *Shindell et al.* [2013] used these TES observations in conjunction with a climate model to

91 separate the climate forcing by ozone loss caused by halocarbons from that of ozone

92 increases caused by air pollution, each of which led to changes in both tropospheric and

93 stratospheric ozone.

94

95 In-situ observations contain too little spatio-temporal information to fully describe the

96 structure and budget of ozone in the UTLS. Operational, nadir-sounding satellite

97 datasets, including the long Solar Backscattered Ultraviolet (SBUV) record, provide

98 climate-quality constraints on total ozone, but do not resolve vertical structure below

99 about 20 km altitude [*Kramarova et al.*, 2013], and therefore do not separate stratospheric

100 and tropospheric ozone from each other. Limb-profiling observations present the best

101 potential for quantifying ozone and its vertical structure through the stratosphere and into

102 the upper troposphere, although the observation errors are typically large below the

103 tropopause, where clouds and water vapor impact radiative transfer. The High-Resolution

104 Dynamic Limb Sounder (HIRDLS) on EOS Aura provides ozone information with ~1 km

105 vertical resolution in the UTLS from 2005-2007 [*Gille et al.,* 2008; *Nardi et al.,* 2008]. It

106 was used by *Olsen et al.* [2010] to study low ozone laminae in the lower stratosphere

107 associated with transport from the tropics to the mid-latitudes. That study found less

108 irreversible transport of ozone in the year with the most filaments, a counterintuitive

109 result that motivates the desire to study year-to-year variability with a longer time series.

110 The vertical resolution of the MLS ozone data used here is ~2.5 km in the UTLS [*Livesey*

111 *et al.,* 2008; *Froidevaux et al.*, 2008] and the vertical resolution of the GEOS-5 model

112 grid is close to 1 km in that layer of the atmosphere. *Olsen et al.* [2008] used the GMI

113 model driven by GEOS-4 assimilated winds at this resolution and showed that the

114 analysis winds have sufficient transport information in the vertical to reproduce a lamina

115 transport event observed by HIRDLS in the lower stratosphere. Case studies done by

116 *Semane et al.,* [2007], *El Amraoui et al.,* [2010], and *Barré et al.* [2013] demonstrated the

117 ability of assimilated ozone data from limb sounders to represent individual deep

118 stratospheric intrusion events. The work delineated above illustrates the value of a multi-

119 year analysis and a statistical evaluation of the capabilities that assimilation of MLS data

120 offers.

121

122 The system used in this study consists of a general circulation model (GCM) and a

123 statistical data analysis module, which will be described in Section 2. Later sections

124 examine the following aspects of UTLS in GEOS-5:

125

126 1. An assessment of the constraints imposed by MLS and OMI observations in the

127   assimilation system, in conjunction with the role of the underlying background

128   (forecast) states generated by the general circulation model (the model component

129   of GEOS-5) informed by assimilated meteorological data (Section 3).

130 2. The realism of the assimilated ozone profiles and partial columns compared to

131   ozonesondes (Section 4).

132 3. An assessment of ozone filaments in GEOS-5, including their structure and

133   frequency of occurrence (Section 5). A validation of the morphology of these

134   events against HIRDLS observations for 2005-2007 is followed by a calculation

135   of interannual variations between 2005 and 2012.

136

137 After these results, the conclusions are linked with an outline of possible applications of

138   GEOS-5 analyses of OMI and MLS ozone.

139   We stress that the assimilated ozone discussed in this study is fundamentally a data-

140   driven product. As such, it is complementary to the output obtained from full-chemistry

141   and transport models such as the Global Modeling Initiative (GMI) project. This work is

142   also an evaluation of the data assimilation system configuration that (after several

143   modifications) will be used in an upcoming Modern-Era Retrospective analysis for

144   Research and Applications version 2 (MERRA-2) reanalysis project currently carried out

145   at NASA's Global Modeling and Assimilation Office.

2. Ozone Assimilation in GEOS-5

This section presents details of the configuration of GEOS-5, focusing on the ozone data and structure of the data assimilation system.

2.1 The GEOS-5 Data Assimilation System

In atmospheric data assimilation, measurements of various components of the state of the atmosphere at a given time are combined with a three-dimensional gridded representation of atmospheric fields obtained from a general circulation model (hereafter: *model*) integration. This is done in a statistically optimal way, by taking into account observational and model forecast errors. This blended new set of fields, termed the *analysis*, is then used to generate an initial condition for a short (here, 6-hourly) model forecast which produces the background fields for the next assimilation cycle. For example, *Kalnay* [2003] and *Cohn* [1997] explain theory of data assimilation in detail. A review of data assimilation methodology applied to chemical constituents, including ozone, can be found in [*Lahoz et al.,* 2007].

The GEOS-5.7.2 DAS is an established configuration of GEOS-5 that was used to generate officially released GEOS-5 data products between August 18, 2011, and June 11, 2013. The "production" configuration ran with a resolution of 0.3125° (longitude) × 0.25° (latitude), with 72 layers between the surface and 0.01hPa. The configuration used in this work has horizontal resolution of 2.5°×2.0° and the same 72 layers. GEOS-5.7.2 includes some scientific advances and enhanced capabilities over GEOS-5.2.0, the

169   version of GEOS-5 used in the Modern-Era Retrospective analysis for Research and

170   Applications MERRA [*Rienecker et al.*, 2011]: improvements to physical processes in

171   the underlying forecast model [*Molod et al.,* 2012] and additional data ingestion

172   capabilities (for newer infrared sounders and for Global Positioning System Radio-

173   Occultation data). The latter were not used to generate the present product. The observing

174   system pertinent to meteorology here is the same as in MERRA.

175

176   The meteorological analysis in GEOS-5 is performed four times daily, using six-hour

177   model forecasts (backgrounds) and observations within a $\pm$3-hour window of the analysis

178   time. The objective of the optimization is to produce an analysis field for which a cost

179   function constructed from the observation-minus-analysis (O-A) residuals is minimized

180   subject to assumed forecast and observation error statistics [*Cohn,* 1997]. The Gridpoint

181   Statistical Interpolation (GSI) [*Wu et al.,* 2002*, Purser et al.,* 2003a,b] optimally

182   combines in-situ observations, retrieved quantities, and satellite-based infrared and

183   microwave radiances along with the backgrounds to produce the analyses. Ozone

184   analyses are impacted only by OMI and MLS observations. In GSI, the analysis of the

185   meteorological fields includes cross-coupling among fields, but ozone is essentially a

186   univariate analysis embedded within the minimization vector. In the configuration used

187   in this study, a climatological ozone field was coupled to the radiation code in the GCM,

188   so the assimilated ozone field did not impact the meteorological forecasts (backgrounds).

189   We found that coupling the assimilated ozone with meteorology instead would not alter

190   the results of this work.

191

192 **2.2 Ozone-specific aspects of GEOS-5**

193 *Chemistry in the GCM*

194

195 The model includes stratospheric ozone production rates and loss frequencies, following

196 *Stajner et al.* [2008]. This month-dependent parameterization was obtained from a two-

197 dimensional chemistry and transport model simulation and corrected using data from the

198 Upper Atmosphere Research Satellite reference climatology. However, the ozone

199 chemistry time scale in the UTLS and in the troposphere is of the order of weeks

200 (compared to daily data insertion) so that in practice the analysis is insensitive to

201 chemistry parameterization in that region. Unlike *Stajner et al.* [2008], tropospheric

202 ozone chemistry has been deliberately simplified in this study: no chemical production or

203 loss is computed and the only removal mechanism is by dry deposition at the surface,

204 derived using a climatological distribution of Normalized Difference Vegetation Index

205 and deposition velocities computed using standard algorithms [*Rienecker et al.*, 2008]. A

206 tropospheric ozone chemistry parameterization is unnecessary because the typical

207 chemical timescales for background ozone in the free troposphere are long compared to

208 the frequency of data insertion in this assimilation (approximately once a day for a given

209 location).

210

211 *OMI observations and their treatment*

212

213 The OMI instrument [*Levelt et al.,* 2006] is a nadir-viewing spectrometer that measures

214 visible and ultraviolet backscattered solar radiation in the 270-550 nm wavelength range

215   with a spectral resolution of ~0.5 nm. The wide swath, of 2600 km, is sampled by a

216   sensor array that covers the cross-track and spectral domains. The 60 cross-track pixels

217   (rows) yield a spatial resolution at nadir of 13 km (along-track) km × 24 km (across-

218   track). The row width increases to about 180 km at the outer extremes [*Levelt et al.,*

219   2006]. The two outer rows on each side of the swath were not used because of large solar

220   zenith angle changes that occur along the wide outer pixels and make the product less

221   accurate. Since 2008, an external blockage has rendered about half of the rows unusable

222   (this is referred to as "row anomaly"). Following guidance from the OMI instrument

223   team (J. Joiner, personal communication) and in the interest of data consistency row

224   numbers 25-60 have been excluded for the entire period of this study, even though the

225   row anomalies did not exist before 2008. The assimilation uses ozone columns retrieved

226   for rows 3-24 of OMI for the entire period. With this row selection the width of the OMI

227   swath is about 1,100 km. The total column observations from OMI are made over the

228   sun-lit atmosphere. In particular, there are no OMI data in the polar night. Only

229   observations made at solar zenith angles less than 84° are used.

230   We use OMI total column ozone retrievals from collection 3 data, version-8.5 retrieval

231   algorithm. An extensive validation of the OMI ozone was done by *McPeters et al.*

232   [2008]. This algorithm is modified from the OMTO3 algorithm previously applied to

233   retrieve data from the Total Ozone Mapping Spectrometer instruments. The use of a

234   more realistic cloud pressure retrieval algorithm [*Joiner and Vasilkov,* 2006] leads to

235   significantly improved total ozone retrievals over cloudy areas compared with earlier

236   versions. A detailed description of the algorithm can be found in the algorithm theoretical

237   basis document available at http://eospso.gsfc.nasa.gov/atbd-category/49. The OMI

238   ozone columns include information from the measurement and climatological a priori

239   information in layers where there is reduced sensitivity of the OMI measurements to

240   ozone. Version 8.5 uses the Labow-Logan-McPeters two-dimensional climatology

241   derived from ozonesonde and satellite data [*McPeters et al.,* 2007]. The a priori provides

242   much of the information in the retrievals in the lower troposphere, where clouds and

243   aerosols affect radiances, and where the sensitivity to ozone is reduced by Rayleigh

244   scattering. To account for these effects, each OMI ozone retrieval includes additional

245   information about the efficiency factors (ε_i) and a priori profiles (y_i^{prior}). These are given

246   on 11 layers, each approximately 5 km thick. An appropriate OMI observation operator

247   has been implemented into the GSI algorithm to ensure that the information content of

248   the OMI data is correctly included. The operator computes the observation-minus-

249   forecast (O-F) residual as:

250   $$O - F = y^o - \sum_{i=1}^{11}[y_i^{prior} + \varepsilon_i(x_i^{forecast} - y_i^{prior})],$$

251

252   where y^o and $x^{forecast}$ denote the retrieved OMI total ozone and the forecast ozone

253   interpolated to the observation location and integrated within each of the 11 layers for

254   which the efficiency factors are provided. The O-F residuals, scaled according to

255   observation and background errors, determine the analysis increment that is added to the

256   background (forecast) ozone to yield the analysis state [*Cohn*, 1997].

257

258   Because the observation density of OMI is substantially larger than the analysis grid, and

259   in order to reduce the large number of observations for computational efficiency, the data

260 are thinned over 150-km grid boxes prior to the analysis. A total of ~12,000 OMI

261 observations per day are assimilated.

262

263 *Assimilation of MLS ozone data*

264

265 MLS measures microwave emissions from the atmospheric limb in a broad spectral

266 region, allowing for retrievals of a large number of trace constituents as well as

267 temperature and pressure [*Waters et al.,* 2006]. This work uses ozone profiles from

268 version 3.3 of the MLS retrieval algorithm [*Livesey et al.,* 2008, 2011], in which ozone

269 information is derived from 25 spectral channels in a spectral band centered at 240 GHz.

270 The ozone mixing ratios from MLS are reported on 55 layers. The 38 layers between 261

271 hPa and 0.02 hPa were used in this work based on recommendations from the MLS

272 science team. The vertical resolution of the MLS ozone data ranges from 2.5 km in the

273 middle stratosphere to 6 km in the mesosphere [*Livesey et al.,* 2008; *Froidevaux et al.,*

274 2008].

275

276 A single MLS profile is a set of discrete point values at retrieval levels. Because the

277 GEOS-5 system represents layer-averaged concentrations, the MLS retrievals were first

278 converted to layer averages on the 37 mid-points (the geometric mean of the pressure

279 values at each two consecutive levels) of the MLS grid. The center of the lowest

280 assimilated layer is thus 237 hPa. The observation operator applied for MLS data in GSI

281 is then a straightforward layer averaging of the background field and spatial interpolation

282 to the observation locations. No attempt has been made to account for the two-

283   dimensional structure of the MLS retrievals: the 200-300 km along-line-of-sight footprint

284   is roughly comparable to the GEOS-5 grid-box size at the resolution used in this work. A

285   pre-assimilation data selection is done following the quality guidelines provided in

286   *Livesey et al.* [2011].

287

288   We emphasize that no bias correction is applied to the MLS data prior to or during

289   assimilation. Instead, the observation errors for MLS ozone are calculated as the square

290   root of the sum of squares of the reported precision and accuracy so that observations

291   with large random or systematic error are given less weight in the assimilation and their

292   impact on the analysis is reduced as a result. For the mid-layer averages, the error is

293   specified as the larger of the values at the two bounding levels. The computed mean

294   observation error in the northern extratropics is about 5% throughout most of the

295   stratosphere down to 75 hPa and increases to about 20% at 237 hPa. We stress that

296   precision errors (given in parts per million by volume) vary from observation to

297   observation. Specific values of the calculated observation error used in the assimilation

298   are available in the assimilation auxiliary output stream.

299

300   A high bias exists for the MLS levels at pressure levels 261 hPa and 215 hPa. Table 1

301   contains the values of the bias separated by four latitude bands evaluated using

302   ozonesondes in 2010 (see Section 4). The relative bias at 261 hPa ranges from 21%

303   between 60°N – 90°N to 46% in the northern middle latitudes. The MLS – sondes

304   differences at 215 hPa are much smaller and disappear at higher levels. The reported

305   accuracy (systematic) error for these levels is higher than for the rest of the assimilated

306   profile. The ~ 20% combined (accuracy with precision) MLS error at the bottom of the

307   profile is large compared to the background error assumed by the assimilation system (at

308   most 10% and as low as 2.5% for tropospheric ozone concentrations, see next

309   subsection). Consequently, the analysis ozone at these levels is dominated by the model

310   values and the impact of MLS observations is less than elsewhere in the stratosphere.

311   This error dependent impact will be evaluated in Section 3.

312

313   *Background error covariances for the ozone analysis*

314

315   When combining the background states with observations, GSI takes into account both

316   observation and background (forecast) errors as well as spatial correlations of the latter.

317   These correlations are used by the analysis algorithm to spread the information from a

318   data location onto its close neighborhood in the horizontal and vertical directions. Since

319   the UTLS ozone exhibits sharp gradients, particularly across the tropopause, the

320   background error covariances should be prescribed with caution in order to avoid

321   excessive smoothing. In older versions of the GSI these correlations were read in from a

322   lookup table. In this work the approach has been modified: Following *Stajner et al.*

323   [2008] and *Wargan et al.* [2010], the background error standard deviation for ozone is

324   assumed to be proportional to the forecast ozone concentration at each grid point. The

325   height-dependent constant of proportionality was tuned using a series of short

326   experiments validated against ozone sonde data and such that the resulting assimilated

327   ozone fields yield smooth zonal and temporal means. In the troposphere, the coefficient

328   is set to 0.1 (i.e. the background error standard deviation is 10% of the local ozone from

329   the latest 6-hourly forecast). The best results were obtained when the coefficient was

330   reduced by a factor of four in the stratosphere relative to the troposphere. For the

331   purpose of this algorithm the tropopause is defined as the 0.1 ppmv ozone isopleth. In

332   particular, the air present in stratospheric intrusions is treated as stratospheric. The

333   primary consequence of this choice of background errors is that relatively large analysis

334   increments in the stratosphere are prevented from excessively affecting the much lower

335   upper concentrations below the tropopause.

336

337   ***Other details of the ozone assimilation***

338

339   In addition to the ozone data screening, the OMI and MLS observations undergo 'online'

340   quality control within the GSI prior to analysis. Values for which the ratio of the

341   calculated observation-minus-forecast (O-F) residual to the observation error is greater

342   than 10.0 are discarded. In practice, this occurs very infrequently: only up to a few MLS

343   observations a day are discarded, most of them in the mesosphere.

344

345   OMI and MLS observations are the only data that impact ozone in this implementation of

346   GEOS-5. Both instruments provide an almost unbroken measurement record during the

347   eight-year period of this analysis, with data gaps that rarely exceed a few days. The major

348   concern is the period from March 27 through April 18, 2011, when MLS data were not

349   available owing to a problem with the instrument. In order to evaluate the potential

350   impacts of the analysis ozone drift resulting from this data gap, an experiment in which

351   MLS observations were turned off was conducted for the same period in 2010 and the

352   results were compared with the full analysis. South of 30°S between 260 hPa and 30 hPa

353   the "no MLS experiment" ozone experiences an approximately linear decrease resulting

354   in concentrations 10%-18% lower then in the MLS analysis after 3 weeks. Between 30°S

355   and 30°N lower stratospheric ozone decreases by ~10% during the first 10 days and

356   stabilizes afterwards. In the northern extratropics there is an alternating pattern of steady

357   decrease (~10% over the first three weeks) and an increase between 200 hPa and 50 hPa

358   by approximately the same amount. In the middle stratosphere there is an increase from

359   10% (30°S - 30°N) to as much as 25% (90°S - 60°S) over the duration of the experiment.

360   In the northern hemisphere these values are smaller: about 3% increase between 30°N

361   and 60°N and a decrease by 3% in the high latitudes. The alternating patterns of

362   increasing and decreasing mixing ratios amount to partial cancellation in the total column

363   as expected from the fact that total ozone is constrained by OMI data in both

364   experiments.

365

366

367

368

369

370   **3. Performance of the GEOS-5 Assimilation System**

371

372   This section shows results describing the GEOS-5 system performance as related to

373   ozone. The purpose is to demonstrate the credibility of the assimilation system and to

374   discuss results that describe the regions where the model and the EOS Aura observations

375   do and do not agree. This is done by examining the spatial distributions, magnitude and

376   behavior of the observation-minus-forecast (O-F) residuals (which measure the

377   discrepancy between the six-hourly model forecast and data) and comparing them with

378   the observation-minus-analysis (O-A) differences. Because, by design, the data

379   assimilation algorithm brings ozone concentrations closer to the observed values the O-A

380   fields are expected to be smaller than the O-Fs. The extent to which this reduction takes

381   place depends on relative magnitudes of observation and background errors.

382

383   Figure 1 shows profiles of the mean and standard deviation of O-F and O-A for MLS

384   ozone mixing ratios in the northern hemisphere extratropics (NH: 30°N-90°N) as a

385   function of pressure for June - August 2010. The standard deviation of O-F increases

386   almost linearly with altitude, from about 0.06 ppmv near 237 hPa to about 0.11 ppmv

387   near 10 hPa. Except at the lowest two layers (centered at 237 hPa and 196 hPa), the mean

388   O-Fs are very small, with weak positive values in the low stratosphere that change sign

389   by the middle stratosphere. Below about 20 hPa the analysis has only a small impact on

390   the mean ozone (the mean O-F and O-A profiles seen in Figure 1(b) are very similar –

391   and close to zero) but there is a clear improvement in the standard deviation (Figure 1(a)).

392   Two separate assimilation experiments, omitting either the MLS or OMI observations

393   were performed. As expected, assimilating only OMI total-column data results in a very

394   different vertical profile in the stratosphere. Assimilating only MLS ozone profiles yields

395   very similar O-Fs in the lower stratosphere, but larger differences in the upper

396   stratosphere, where timescales for photochemistry are short. This is expected given the

397   approximate parameterized chemistry scheme used in the model.

398

399   A zonal-mean section of the seasonally averaged O-Fs for JJA 2010 (Figure 2) illustrates

400   in more detail the nature of the assimilation. The largest differences are evident in the

401   upper stratosphere and these are positive over much of the globe, meaning that the six-

402   hour forecasts are biased low compared to the observations. However, the mean O-F of

403   about 0.2 ppmv in Figures 1 and 2 is also of comparable magnitude to the MLS data error

404   (not shown), indicating that the error has not grown to unacceptable values in the course

405   of the six-hour forecast. A deep band of negative O-Fs is prominent at all levels above

406   10 hPa at southern latitudes, but the zonal-mean ozone O-Fs are smaller than the MLS

407   observation errors everywhere in the stratosphere. The O-Fs in the upper stratosphere

408   represent a relatively small contribution to the integrated column amounts because of

409   small air density there. While the vertically integrated zonal mean MLS O-Fs range

410   between ~-1.2 Dobson Units (DU or m. atm. cm) to about 4.8 DU depending on latitude,

411   the upper stratospheric portion (5 hPa to the top of the MLS profile) contributes between

412   -0.2 DU to 0.6 DU.

413

414   Spatial maps of the O-F and O-A distributions for stratospheric partial columns in June -

415   August 2010 from MLS in DU are shown in Figure 3(a) and 4(a), respectively. These

416   seasonal maps were computed off-line using the six-hourly information from the

417   analyses. In these computations, and throughout this study (except the ozone-based

418   criterion used in the definition of background errors and discussed in Section 2.2), the

419   tropopause is diagnosed differently in the tropics and the extratropics. In the 10°S –

420   10°N latitude band, the tropopause pressure is assumed to be 100hPa. Elsewhere, a

421   dynamic definition is used, based on the potential vorticity expressed in "Potential

422   Vorticity Units" (where one PVU = 10^{-6} K m^2 s^{-1} kg^{-1}). Following *Holton et al.,* [1995]

423   the pressure of the 2 PVU isopleth is used as the tropopause.

424

425   The mean O-F for the stratospheric ozone column (Figure 3(a)) reveals positive values,

426   with the six-hour forecasts containing less ozone than in the MLS observations, at almost

427   all locations, the exceptions being widespread areas with negative values at southern high

428   latitudes and smaller regions with weaker negative values over the tropical Atlantic

429   Ocean, the north-east part of the North American continent, South East Asia, and the

430   Arabian Peninsula. This is broadly consistent with the zonal-mean O-Fs in Figure 2, but

431   illustrating some zonal asymmetries. The high O-F bias in the northern middle latitudes

432   and elsewhere arises from the mean profile shape in Figures 1 and 2, where the positive

433   O-Fs between 200 hPa and 100 hPa along with the increased air density make these

434   layers the dominant contributors to the stratospheric partial-column O-F. The analysis

435   tends to reduce these systematic biases, with O-As systematically smaller than the O-Fs

436   in all locations as shown in Figure 4(a). The remaining, tropospheric portion of the MLS

437   partial column O-F between 237 hPa (wherever the tropopause lies above that level) and

438   the tropopause is shown in Figure 3(b). The values range from 0 DU to 2 DU with largest

439 O-Fs over the Atlantic, Africa, the Indian Ocean and between Australia and South

440 America.

441

442 Figure 3(c) shows the spatial distribution of the O-F field for OMI total ozone for June -

443 August 2010, computed according to Equation (1). There are several features of note,

444 discussed in turn.

445

446 1. The O-F residuals are generally positive over land, especially in regions known to

447   be dominated by strong pollution. For example, patches of large positive O-Fs

448   over the west coast of equatorial Africa and in eastern parts of Asia are located in

449   regions known to have strong tropospheric ozone precursor emissions from

450   biomass burning and anthropogenic emissions. The O-F fields reflect the fact that

451   these ozone production sources are absent in the model.

452 2. Over much of the Pacific the O-F for total ozone is negative. The strongest

453   negative values are aligned with regions of intense precipitation, including the

454   Intertropical Convergence Zone, the South Pacific Convergence Zone and the

455   Monsoon Trough over the Maritime continent. This suggests that either there is

456   too little lofting of ozone-poor air from the maritime boundary layer in the model

457   or that the air being lofted has more ozone than in the real atmosphere. There

458   exists evidence for the convective transport being too shallow in at least the

459   MERRA version of the GEOS-5 model [*Wright and Fueglistaler,* 2013]

460 3. A prominent band of positive O-Fs is evident over the Southern Ocean, at the

461   seasonal extreme of the OMI observations. In this region the ozone observations

462   are made at high solar zenith angles and are have larger uncertainty than

463   elsewhere. The strong positive O-Fs for OMI are, however, collocated with the

464   band of negative O-Fs for MLS stratospheric partial columns (Figure 3(a)). All of

465   these features carry, with smaller magnitudes, into the corresponding O-A fields.

466   This leakage of a potential error in the OMI observations into the stratosphere of

467   the analysis suggests that the OMI data are being given too much weight in the

468   analysis system at these latitudes. Future work will address this potential

469   discrepancy, by increasing the observation error on OMI data near the polar night.

470   Over elevated terrain (e.g., the Andes, the Rocky Mountains, and the Himalayan

471   Plateau) there are prominent regions of negative O-F in the OMI data. This is a

472   consequence of the fact that the climatological a priori ozone values used in the

473   retrievals are zonally symmetric and therefore overestimate the a priori ozone

474   over elevated areas (G. Labow, personal communication, 2013). Since the

475   analysis subtracts the a priori, as described in Section 2, large negative O-Fs arise.

476   It is an artifact of the settings and data used.

477   The corresponding O-As are shown in Figure 4 for reference. As expected the

478   assimilation leads to reductions of the model – observations discrepancies. One

479   noteworthy aspect in Figures 3 and 4 is the fact that the O-As for the upper tropospheric

480   portion of MLS observations are almost unchanged from the positive values of the O-Fs

481   as seen by comparing panels (b) of both figures. This arises from the larger error values

482   for MLS ozone in this region and the use of the OMI data alongside MLS in the analysis.

483   The outcome that the analysis does not draw to the MLS observations in the upper

484   troposphere means that the O-As remain high there – the known high bias quantified in

485   Table 1 in the MLS V3.3 retrievals (see Section 2) has a negligible impact on the analysis

486   owing to the large observation errors.

487

488   These features illustrate an overall success of the GEOS-5 analysis in matching the OMI

489   and MLS observations with the model backgrounds, yet also point to regions where the

490   assimilation system (including the use of the input observations) need improvements in

491   the future.

492

493   The final part of this evaluation considers the time series of O-F and O-A statistics

494   through 2010 (Figure 5). Seasonal variations in the stratospheric partial column from

495   MLS demonstrate the success of the analysis in reducing the background errors (to the

496   levels determined by the MLS data accuracy). A similar error reduction is evident for the

497   OMI weighted total-column O-Fs, where the O-As are reduced to around zero for the

498   entire year. Consistent with the discussion of MLS errors, there is very little reduction of

499   the MLS O-Fs in the upper troposphere (panel (b)).

500

501

502

503

504 **4. Validation using Independent Ozone Observations**

505

506 This section presents the results of comparisons between the assimilated ozone data and

507 independent observations from ozonesondes at a variety of locations, mostly over

508 northern hemisphere and tropical landmasses (Figure 6). Following a discussion of the

509 stratospheric ozone column, the main focus is on the lower stratosphere (LS), defined as

510 the atmospheric layer between the tropopause and the 50-hPa surface, and the upper

511 troposphere (UT), the layer between the 500-hPa surface and the tropopause. The entire

512 troposphere is examined in detail by *Ziemke et al.* [2014]. It is important to keep in mind

513 that the analysis ozone at any given grid-point represents the grid-box average rather than

514 a point value and therefore it does not account for the variability of the ozone field within

515 that box. Some differences between the analyses and the sondes may be due to differing

516 air masses arising from spatial and temporal mismatches, as well as horizontal

517 displacement of the sonde far from its launch location as a it ascends.

518 **4.1 Comparison with ozonesonde observations at Hohenpeissenberg**

519

520 Ozone sondes are launched regularly at the Hohenpeissenberg station (47°48'N, 11°E),

521 providing the dense time series of in-situ observations that has been studied in detail by

522 *Steinbrecht et al.* [1998] and references therein. This subsection compares the analyzed

523 fields with the Hohenpeissenberg record, using 1016 soundings between the years 2005

524 and 2012. This evaluation examines ozone changes associated with a transport event in

525 late March 2007, followed by a more rigorous statistical comparison for the eight-year

526 period of this analysis.

527

528 Figure 7 shows the evolution of the analysis ozone and potential vorticity from GEOS-5

529 over Hohenpeissenberg between March 15 and 31, 2007. High ozone and PV values

530 between March 19 and March 25 mark the passage of a cyclonic anomaly from higher

531 latitudes over this location. At 100 hPa, ozone sharply increases from about 10 mPa to

532 about 18 mPa on March 19, and similar increases are evident over the 200 hPa - 70 hPa

533 layer. A simultaneous increase of the pressure of the 2 PVU isopleth denotes a sharp

534 drop in the tropopause altitude at this time. Four soundings from Hohenpeissenberg are

535 available for the evaluation. These took place on March 14, 22, 23, and 28, 2007. Ozone

536 partial pressures from the sondes and the GEOS-5 analyses (Figure 8) reveal the success

537 of the analysis in capturing the changing shape of the ozone profile, especially the large

538 increase of ozone in the 200-70hPa layer on March 22. The spacing of the GEOS-5

539 levels is about 1 km near the tropopause so the finest scales of the vertical ozone

540 variations are not captured in the analyses: examples are a narrow feature in the sonde

541 data near 50 hPa on March 22 and the oscillatory structure on March 28. We emphasize

542 again that sondes measure point values while the analysis represents grid-cell mean ozone

543 concentrations. However, the analyses capture the sharp vertical gradients seen in Figure

544 8 above the tropopause very well.

545

546 The remainder of this section focuses on comparisons of tropopause to 50 hPa columns,

547 as these de-emphasize the smaller vertical scales.

548

549   Figure 9 compares the integrated LS ozone column from GEOS-5 with the

550   Hohenpeissenberg sondes over 2005-2012.   Such comparisons are made by first

551   horizontally interpolating the GEOS-5 ozone concentrations to the sonde location and

552   then integrating both profiles in the vertical to obtain LS and UT columns. The analysis

553   time closest to the sounding is used so that the time separation never exceeds three hours.

554   Transport events like that in March 2007 occur often in this record and Figure 9

555   illustrates the broad competency of the analysis in capturing such excursions from the

556   smoother seasonal cycle as seen by comparing the time series of Hohenpeissenberg data

557   and sonde-analysis differences. There is an overall good agreement between the analysis

558   and the sonde data: the mean sonde-minus-analysis difference and the standard deviation

559   are 1.43 DU and 8.1 DU, respectively. However, the bias varies from year to year, from -

560   3.94 DU (-3.86%) in 2005 to 3.79 DU (3.44%) in 2009. The correlation between sondes

561   and analysis is 0.98. The distributions of the sonde data and analysis (panel (b)) exhibit

562   similar behavior: a maximum at about 70 DU and long tail at high values. The

563   Kolmogorov-Smirnov test yields a p-value of 0.44 providing strong support to the

564   hypothesis that the two samples are drawn from the same probability distribution. The

565   distribution of the sonde-analysis differences, shown in panel (d), is close to Gaussian

566   with some outliers on the positive side. Stratospheric ozone column in the middle

567   latitudes exhibits an annual cycle with a springtime maximum resulting from transport of

568   ozone from its photochemical source in the tropical stratosphere by the Brewer-Dobson

569   circulation. This annual cycle is modulated by large year-to-year variability and high-

570   frequency changes due to varying synoptic conditions. This large spectrum of variability

571   seen in the sonde data is closely matched by ozone from the assimilation.

4.2 Statistical comparisons with ozonesondes

The evaluation presented using Hohenpeissenberg data illustrates the vital role of in-situ observations to evaluate the global ozone analyses. About 16,000 Electrochemical Concentration Cell (ECC) sonde observations are available between 2005 and 2012, on the inhomogeneous network shown in Figure 6. The main data sources are the archives from the Network for the Detection for Atmospheric Composition Change (NDACC) (http://www.ndsc.ncep.noaa.gov/) and the Southern Hemisphere Additional Ozonesondes (SHADOZ) [*Thompson et al.,* 2003]. Additional data from field campaigns are also included in this comparison. Note that with the exception of the Antarctic stations, almost no observations are available south of the southern hemisphere subtropics. *Komhyr et al.* [1995] found that the ECC precision was of the order of ±5% in the region between 200 hPa and 10 hPa. Below 200 hPa, the precision is estimated to be between –7% and +17%, with the higher errors found in the presence of steep gradients and where ozone concentrations are near zero. More recent chamber experiments (conducted in the environmental simulation facility at the Research Centre Juelich) revealed precision estimates better than ±(3–5)% and an accuracy of about ±(5–10)% up to 30 km altitude [*Smit et al.*, 2007].

Figure 10 shows the distribution of sonde-to-analysis ozone comparisons for the UT and the LS, using all sondes between 2005 and 2012. The vertical extents of the UT and LS layers are computed for each analysis time from the GEOS-5 meteorological fields as defined in Section 3 and are the same for the analysis and sonde data. In the LS, the

595   analysis is higher than the sonde data by 0.5 DU (about 0.5%) and the standard deviation

596   of the differences is 8.63 DU (Figure 10(b)). The dependence of these statistics on the

597   latitude band is summarized in Table 2. The largest bias is found in the tropics (8.85%)

598   and the smallest in the northern middle latitudes (less than 0.5%). The correlation

599   between the two data sets is 0.99, indicating that the assimilation system accurately

600   represents the variability and distributions of LS ozone partial columns. The shape of the

601   distribution of the sonde-minus-analysis differences (Figure 10(b)) departs from Gaussian

602   slightly, with a more narrow maximum and fatter tails. The fat positive tail is explained

603   by occasional large positive excursions seen in the sonde data but not fully captured by

604   this 2°×2.5° analysis. A number of such events are evident in Figure 9(a) in the form of

605   sharp spikes in the sonde time series.

606

607   Typical column values in the UT are an order of magnitude smaller than in the LS and

608   this gradient is captured by the assimilation (Figure 10(c)). This demonstrates that the

609   assimilation reproduces sharp vertical gradients in the tropopause region despite

610   relatively low vertical resolution of the assimilated data. Analyzed ozone in the UT is

611   biased low by 1.16 DU (9.26%) with respect to the sondes. The standard deviation of the

612   differences and the correlation coefficient are 2.82 DU and 0.87, respectively. These

613   statistics have some latitudinal dependence, as summarized in Table 3. The best

614   agreement is in the northern high and middle latitudes. The discrepancy between the

615   analysis and sonde data is largest in the tropics, however, we stress that the data sampling

616   is sparse south of 30°N.

617

618   Figure 11 and Table 4 show the seasonal dependence of the UT comparisons computed

619   from all available data. The best agreement with sondes is in December-February and

620   March-May when the relative bias with respect to sonde data is about 7% and 8%,

621   respectively. In the other two seasons the bias and standard deviation of the sonde –

622   analysis differences are higher, however the correlation coefficient remains high at 0.81

623   (June-August) and 0.88 (September-November).

624

625   There is also some interannual variability in sonde and analysis statistics, illustrated by

626   time series of annual mean and standard deviation of the sonde data and sonde – analysis

627   differences in different latitude bands (Figure 12). In the northern extratropics the bias

628   and standard deviation of differences vary by about 1 DU between years. Between 30°S –

629   30°N these numbers are close to about 2 DU for the bias and standard deviation. Standard

630   deviations of the sonde-minus-analysis differences are consistently less than those of the

631   sonde data in each year, indicating the presence of useful information in the analysis.

632

633   While these comparisons focus on latitudes north of 30°S, we will briefly discuss the

634   southern high latitudes. In June, July and August the analysis ozone in the LS is biased

635   high by 3.81 DU with respect to sondes south of 60°S. The bias is 3.34 % of the mean

636   sonde ozone. The standard deviation of the differences is 9.89 DU and the sonde –

637   analysis correlation is 0.93 (0.83 in the UT). This high bias is larger than anywhere north

638   of 30°S and larger than the global average (-0.5 DU), consistent with strongly positive

639   analysis increments along the coast of Antarctica resulting from large O-Fs discussed in

640   Section 3.

641

4.3 Summary of the Evaluation

643

This section has demonstrated that the ozone distribution in GEOS-5, when MLS and

OMI retrievals are assimilated, is in excellent agreement with the sonde observations in

the lower stratosphere. That evaluation extends the results of *Stajner et al*. [2008], who

found stratospheric columns that were in good accord with Stratospheric Aerosol and Gas

Experiment (SAGE-II) observations when MLS and OMI data were assimilated into an

offline system driven by GEOS-4 meteorology.

650

Constraining upper tropospheric ozone in GEOS-5 through data assimilation is an

emerging capability. Low biases in the tropospheric ozone have been reported in other

data products derived from OMI and MLS observations using tropospheric residual

techniques, most recently by *Ziemke et al*. [2014]. The bias there arises from the high

bias in the lowest used levels of MLS, quantified in Table 1, that gets subtracted from the

OMI total ozone resulting in an underestimation in the troposphere. This is not the

primary cause of the low tropospheric bias in this analysis because, as shown in previous

sections, owing to relatively large observation errors assigned to the lowest UTLS levels

the MLS bias has very little (if any) impact on the analysis. In particular, comparisons

with ozonesondes reveal only a 0.5 DU (0.5%) positive bias in the LS. In the real world,

UT ozone has several sources: transport of ozone-rich air from urban pollution sources, in

situ production from odd-nitrogen family produced by lightning, and stratospheric

intrusions. While the latter process is included in the current GEOS-5 system (limited by

664   its capability to resolve the fine-scale features of the intrusions), the others are not. The

665   present runs did not use a tropospheric chemistry mechanism, so in-situ sources of ozone

666   through lightning- and pollution-induced NO_x sources are absent. Surface emissions of

667   ozone precursors are not included and details of their impacts on UT ozone also require a

668   more thorough investigation of convective transport in GEOS-5. In addition, the

669   sensitivity of OMI data to ozone the lowermost troposphere is limited, leading to

670   underestimated ozone mixing ratio below the 500 hPa pressure level – and, through

671   transport, in the UT. The importance of the lower stratosphere in this context is

672   reinforced by the results of *Ziemke et al.* [2014] who found that the analysis is lower than

673   ozonesondes by 3.99 DU globally compared to 1.16 DU in the UT as shown here. It

674   follows that the analysis underestimates ozone below 500 hPa by over 2.8 DU – the bulk

675   of the error arises from the lower troposphere.

676

677   Despite the shortcomings, the current form of the GEOS-5 ozone assimilation system

678   does accurately capture the character of the sharp ozone gradients around the tropopause,

679   thus delineating between stratospheric and tropospheric ozone fields.

680

681

682

683

684

685

686

5. Ozone Laminae near the Tropopause

Ozone fields near the tropopause display a highly variable structure. The irreversible transport of stratospheric air into the troposphere is a source of tropospheric ozone (*Olsen et al*. [2004] and references therein). In the lower stratosphere the ozone budget is affected by the occurrence of low-ozone laminae, created by the poleward isentropic transport of tropical air by planetary waves [*Dobson,* 1973]. Such laminae have been identified by *Olsen et al.* [2010] in ozone retrievals from HIRDLS [*Gille et al.,* 2008*; Nardi et al.,* 2008]. The high vertical resolution (~1 km) of HIRDLS data provides information on ozone laminar structures in the UTLS unavailable from lower vertical resolution limb sounders. Given that the vertical grid of GEOS-5 has a spacing of about 1 km in the UTLS, it is reasonable to expect that the resolved vertical scales defined by the transport field may represent such laminae, even though the MLS vertical grid is too coarse to resolve them. This expectation is supported by the results of *Olsen et al.* [2008] who studied an example of intrusion of lower stratospheric tropical air into the northern middle latitudes in January 2006 and demonstrated that the GMI chemistry and transport model driven by assimilated wind fields reproduced the feature in an excellent agreement with HIRDLS observations. Their model had the same vertical and horizontal resolution as the GEOS-5 GCM used in this study.

Figure 13 shows two laminar structures in the ozone field on April 8 and April 15, 2007. The plots compare structures retrieved from HIRDLS measurements with those from collocated GEOS-5 analysis ozone in the northern middle latitudes. Both data sets were

710   interpolated to isentropic vertical coordinates for this comparison The examples show

711   thin low-ozone layers separating the stratospheric air from ozone-rich filaments below.

712   On both days, the GEOS-5 analysis reproduces the overall shape of these structures as

713   well as sharp gradients between stratospheric and upper-tropospheric ozone content. On

714   April 15, the maximum vertical gradient at the minimum ozone mixing ratio is nearly

715   horizontal between 40°N – 50°N in the constant potential temperature coordinate,

716   indicating isentropic transport of air from lower latitudes. The thickness of these low

717   ozone layers is about 1 km; this is approximately the vertical resolution of the analysis in

718   the UTLS (~1.1 km above 200 hPa and ~0.8 km immediately below) and should be

719   contrasted with much coarser resolution of the MLS data (2.5 km – 3 km).

720

721   An automated low-ozone lamina detection algorithm was applied to the HIRDLS data

722   and the along-track collocated analysis. This methodology is described in detail in *Olsen*

723   *et al.* [2010]. The algorithm identifies low ozone layers by applying the following

724   criteria:

725   • The difference between the ozone concentration at the base of the lamina and the

726   minimum ozone concentration within the layer (*magnitude*) must be greater than

727   the sum of HIRDLS precisions at these locations.

728   • The difference between potential temperature at the layer top and bottom

729   (*thickness*) must not exceed 60 K (about 2.5 km).

730   • A structure is registered as a low-ozone lamina if it is consistent across at least

731   three consecutive HIRDLS profiles.

732

733   Zonal low ozone laminae counts for February and April 2007 are shown in Figure 14.

734   There is an overall agreement in the spatial distribution of the number and vertical extent

735   of the laminae between HIRDLS and the assimilation, except at lower levels (380 K –

736   400 K) where the counts are underestimated in the analysis. This result implies that ozone

737   transport in the stratosphere is well represented in the analysis but the structure near the

738   tropopause and, in particular the quality of cross-tropopause transport requires further

739   evaluation. We note that, some features in HIRDLS profiles that are identified as laminae

740   may be due to noise in the retrievals [*Olsen et al.,* 2010]. The maximum number of low-

741   ozone laminae occurs between 400 K and 460 K in April. The vertical distribution of the

742   laminae detected in the HIRDLS data is more compact in April than in February. Both of

743   these characteristics from the HIRDLS data are reproduced in the analysis. The total

744   number of detected laminae is underestimated in the analysis in both months, but the

745   statistics of laminae thickness and magnitude (defined as the relative difference between

746   the maximum and minimum ozone mixing ratio across a lamina) are very close in both

747   data sets (see Table 5).

748

749   An eight-year long record of the annual mean number of low ozone laminae (expressed

750   as number of laminae per day) from the analysis is shown in Figure 15 along with results

751   from HIRDLS data for the first three years. The analysis displays notable interannual

752   variability with the maximum number of laminae in 2006 associated with a major

753   stratospheric sudden warming that occurred in that year. This is consistent with the data

754   and the results of *Olsen et al.* [2010]. Similar to the monthly statistics above, the mean

755 number of laminae is less by 5 – 8 per day in the analysis than in HIRDLS data but the

756 interannual differences are captured at least qualitatively.

757

758

759

760

761

762

763

764

765

766

767

768

769

770

771

772

773

774

6. Conclusions and Discussion

A new global ozone product was obtained by assimilating EOS Aura OMI and MLS data into a GEOS-5 DAS for 2005 through 2012. This expands on prior experiments in which EOS Aura observations were assimilated into GEOS-4 [*Stajner et al.*, 2008; *Wargan et al.*, 2010] for a much shorter period. The focus of this work was on the fidelity of ozone distributions in the upper troposphere and lower stratosphere (UTLS).

As demonstrated in Section 3 the MLS profile data act in the assimilation system to constrain the analysis stratosphere and their impact is weighed according to the combination of background and observation errors. In particular, the impact of the lowest MLS levels, where there is a positive bias in the data, is less than elsewhere. With the stratospheric ozone constrained by MLS, the observation – forecast residuals for OMI display a structure consistent with deficiencies of the model in the troposphere: underestimation of ozone over land and a low bias over ocean, especially in regions of strong convection.

Compared to ozonesondes, the GEOS-5 analysis performs extremely well in the lower stratosphere. The bias and standard deviation of the assimilation – sonde differences are within about 1% and 10%, respectively, and the correlation between the two data sets is 0.99. A larger, season-dependent bias (9%– 14%) exists in the upper troposphere but the correlation is still high, over 0.8, indicating an accurate representation of the analysis ozone variability. The fact that the analyzed ozone in the UT is not as good as the LS is

798 expected because stratospheric chemistry is adequately represented in the model, while in

799 the troposphere important ozone sources are absent. This introduces a low bias in the

800 model forecast ozone that is subsequently propagated into the analysis. Any bias that

801 originates in the lower troposphere is not likely to be completely corrected by

802 assimilation because of low sensitivity of backscattered UV signal to the lowermost

803 atmosphere.

804

805 The analysis of transport-related low-ozone laminae in the tropopause region in the

806 GEOS-5 analyses of MLS and OMI data demonstrates a moderate success of this system.

807 Given that the high-resolution HIRDLS profiles are available for only three years, the use

808 of the MLS+OMI assimilation to extend this record is of some value. Although the

809 present system underestimates the number of laminae by about 20% compared to

810 HIRDLS, it is possible that this will improve in future GEOS-5 systems with a higher

811 vertical resolution near the tropopause (in planning), especially when used with a finer

812 horizontal scale, as in near-real-time and reanalysis [e.g., *Rienecker et al.*, 2011]. In

813 addition, an independent estimate of the lamina statistics is desirable since some of the

814 features derived from HIRDLS may be spurious [*Olsen et al.,* 2010] The present study

815 opens opportunities for analyzing the details of the UTLS tracer transport processes, -

816 complementary to model studies.

817

818 Given the limited vertical resolution of MLS, we conclude that the high correlation

819 between the analysis ozone and sonde observations as well as the accurate representation

820 of laminae is a consequence of the fidelity of transport driven by assimilated GEOS-5

821 meteorological fields.

822

823 This study has presented a benchmark of a complex assimilation system that projects

824 along-track satellite observations to high-frequency global maps of ozone. A companion

825 study [*Ziemke et al.,* 2014] examines the integrity of tropospheric ozone maps computed

826 from the assimilated products in this work with those using other methods. The primary

827 conclusion of that work was that the GEOS-5 assimilation was the best method of

828 deriving tropospheric ozone fields from OMI and MLS owing to the frequency and

829 continuity of the records it produces and its vertical resolution. Future studies using this

830 GEOS-5 system, or modifications of it, will address tracer transport in the UTLS in the

831 presence of stratospheric sudden warmings and interpretation of the upper tropospheric

832 ozone content in a dynamical framework. This product can be also used as a priori in

833 ozone retrieval algorithms in radiance data processing and in research examining

834 radiative forcing by ozone.

835

836 The success of this experiment provides a strong justification for assimilating the MLS

837 and OMI ozone observations in atmospheric reanalyses. Consequently, these data will be

838 used in MERRA-2, the follow-on to the MERRA reanalysis [*Rienecker et al.,* 2011].

850

851

852

853

854

855

856

857

858

859   **References**

860

861   Barré, J., El Amraoui, L., Ricaud, P., Lahoz, W. A., Attié, J.-L., Peuch, V.-H., Josse, B.,

862   and Marécal, V. (2013) Diagnosing the transition layer at extratropical latitudes using

863   MLS O_3 and MOPITT CO analyses, Atmos. Chem. Phys., 13, 7225-7240,

864   doi:10.5194/acp-13-7225-2013.

865

866   Cohn, S.E. (1997), An Introduction to Estimation Theory. J.Met.Soc of Japan, Vol. 75,

867   No. 1B, pp. 257 – 288.

868

869   Dobson, G. M. B. (1973), The laminated structure of the ozone in the atmosphere, Q. J.

870   R. Meteorol. Soc., 99, 599–607.

871

872   Duncan, B. N., J. J. West, Y. Yoshida, et al. (2008) The influence of European pollution

873   on ozone in the Near East and northern Africa, Atmos. Chem. Phys., 8, 22-2283.

874

875   El Amraoui, L., Attié, J.-L., Semane, N., Claeyman, M., Peuch, V.-H., Warner, J.,

876   Ricaud, P., Cammas, J.-P., Piacentini, A., Josse, B., Cariolle, D., Massart, S., and

877   Bencherif, H. (2010). Midlatitude stratosphere – troposphere exchange as diagnosed by

878   MLS O_3 and MOPITT CO assimilated fields, Atmos. Chem. Phys., 10, 2175-2194,

879   doi:10.5194/acp-10-2175-2010.

880

881 Froidevaux, L., et al. (2008), Validation of Aura Microwave Limb Sounder stratospheric

882 ozone measurements, J. Geophys. Res., 113(D15), D15S20, doi:10.1029/2007JD008771.

883

884 Gille, J., et al. (2008), High-resolution dynamics limb sounder: Experiment overview,

885 recovery, and validation of initial temperature data, J. Geophys. Res., 113(D16), D16S43,

886 doi:10.1029/2007JD008824.

887

888 Holton, J. R., P. H. Haynes, A. R. Douglass, R. B. Rood, and L. Pfister (1995),

889 Stratosphere-troposphere exchange, Rev. Geophys., 33(4), 403–439.

890

891 Joiner, J. and Vasilkov, A. P.: First results from the OMI Rotational Raman Scattering

892 Cloud Pressure Algorithm, IEEE T. Geosci. Remote, 44, 1272–1282, 2006.

893

894 Kalnay, E. (2003). Atmospheric Modeling, Data Assimilation and Predictability.

895 Cambridge Univ. Press

896

897 Komhyr W. D., R. A. Barnes, G. B. Brothers, J. A. Lathrop, J. B. Kerr, and D. P.

898 Opperman (1995), Electrochemical concentration cell ozonesonde performance

899 evaluation during STOIC 1989. J. Geophys. Res. 100: 9231–9244.

900

901 Kramarova, N., P. K. Bhartia, S. Frith, R. McPeters, and R. Stolarski (2013), Interpreting

902 SBUV smoothing errors: An example using the Quasi-biennial oscillation, Atmos. Meas.

903 Tech. Discuss., 6, 2,721–2,749, doi:10.5194/amtd-6-2721-2013.

904 Lacis, A., D.J. Wuebbles, and J.A. Logan (1990) Radiative forcing of climate by changes

905 in the vertical distribution of ozone. J. Geophys. Res. 95, 9971-9981.

906

907 Lahoz, W. A., Errera, Q., Swinbank, R., and Fonteyn, D. (2007) Data assimilation of

908 stratospheric constituents: a review, Atmos. Chem. Phys., 7, 5745-5773, doi:10.5194/acp-

909 7-5745-2007.

910

911 Levelt, P. F., G. H. J. V. D. Oord, M. R. Dobber, A. Mälkki, H. Visser, J. D. Vries, P.

912 Stammes, J. O. V. Lundell, and H. Saari (2006), The Ozone Monitoring Instrument, IEEE

913 Trans. Geosci. Remote Sens., 44, 1093–1101, doi:10.1109/TGRS.2006.872333.

914

915 Livesey, N. J., et al. (2008), Validation of Aura microwave limb sounder O_3 and CO

916 observations in the upper troposphere and lower stratosphere, J. Geophys. Res.,

917 113(D15), D15S02, doi:10.1029/2007JD008805.

918

919 Livesey N. J., W. G. Read, L. Froidevaux, A. Lambert, G. L. Manney, H. C. Pumphrey,

920 M. L. Santee, M. J. Schwartz, S. Wang, R. E. Cofield, D. T. Cuddy, R. A. Fuller, R. F.

921 Jarnot, J. H. Jiang, B. W. Knosp, P. C. Stek, P. A. Wagner, and D. L. Wu. (2011).

922 Version 3.3 Level 2 data quality and description document. Available at

923 http://mls.jpl.nasa.gov/data/v3-3_data_quality_document.pdf

924

925 McPeters, R. D., G. J. Labow, and J. A. Logan (2007), Ozone climatological profiles for

926 satellite retrieval algorithms, J. Geophys. Res., 112, D05308,

927   doi:10.1029/2005JD006823.

928

929   McPeters, R. D., et al. (2008). Validation of the Aura Ozone Monitoring Instrument total

930   column ozone product, *J. Geophys. Res.*, **113**, D15S14, doi:10.1029/2007JD008802.

931

932   Molod, A., L. Takacs, M. Suarez, J. Bacmeister, I.-S. Song, and A. Eichmann (2012).

933   The GEOS-5 Atmospheric General Circulation Model: Mean Climate and Development

934   from MERRA to Fortuna. *NASA Technical Report Series on Global Modeling and Data*

935   *Assimilation, NASA TM—2012-104606*, Vol. 28, 117 pp.

936

937   Nardi, B., et al. (2008), Initial validation of ozone measurements from the High

938   Resolution Dynamics Limb Sounder, J. Geophys. Res., 113(D16), D16S36,

939   doi:10.1029/2007JD008837.

940

941   Olsen, M. A., M. R. Schoeberl, and A. R. Douglass (2004), Stratosphere-troposphere

942   exchange of mass and ozone, J. Geophys. Res., 109, D24114,

943   doi:10.1029/2004JD005186.

944   Olsen, M. A., A. R. Douglass, P. A. Newman, J. C. Gille, B. Nardi, V. A. Yudin, D. E.

945   Kinnison, and R. Khosravi (2008), HIRDLS observations and simulation of a lower

946   stratospheric intrusion of tropical air to high latitudes, Geophys. Res. Lett., 35, L21813,

947   doi:10.1029/2008GL035514.

948   Olsen, M. A., A. R. Douglass, M. R. Schoeberl, J. M. Rodriquez, and Y. Yoshida (2010),

949   Interannual variability of ozone in the winter lower stratosphere and the relationship to

950   lamina   and   irreversible   transport,   J.   Geophys.   Res.,   115,   D15305,

951   doi:10.1029/2009JD013004.

952

953   Purser, R. J., W.-S. Wu, D. F. Parrish, and N. M. Roberts (2003a), Numerical aspects of

954   the application of recursive filters to variational statistical analysis. Part I: spatially

955   homogeneous and isotropic Gaussian covariances, Mon. Wea. Rev., 131, 1524-1535.

956   Purser, R. J., W.-S. Wu, D. F. Parrish, and N. M. Roberts (2003b), Numerical aspects of

957   the   application   of   recursive   filters   to   variational   statistical   analysis.   Part   II:

958   spatially inhomogeneous and anisotropic general covariances, Mon. Wea. Rev., 131, pp.

959   1536-1548.

960

961   Randel, W. J., F. Wu, and P. Forster (2007). The extratropical tropopause inversion layer:

962   Global observations with GPS data, and a radiative forcing mechanism. J. Atmos. Sci.,

963   64, 4489–4496.

964   Rienecker, M.M., M.J. Suarez, R. Todling, J. Bacmeister, L. Takacs, H.-C. Liu, W. Gu,

965   M. Sienkiewicz, R.D. Koster, R. Gelaro, I. Stajner, and J.E. Nielsen (2008). The GEOS-5

966   Data Assimilation System— Documentation of Versions 5.0.1, 5.1.0, and 5.2.0, NASA

967   Tech. Memo (2008) NASATM-2008-104606.

968   Rienecker, M.M., M.J. Suarez, R. Gelaro, R. Todling, J. Bacmeister, E. Liu, M.G.

969   Bosilovich, S.D. Schubert, L. Takacs, G.-K. Kim, S.E. Bloom, J. Chen, D. Collins, A.

970   Conaty, A. da Silva, W. Gu, J. Joiner, R.D. Koster, R. Lucchesi, A. Molod, T. Owens, S.

971   Pawson, P. Pegion, C.R. Redder, R. Reichle, F.R. Robertson, A.G. Ruddick, M.

972   Sienkiewicz, J. Woollen (2011), MERRA - NASA's Modern-Era Retrospective Analysis

973   for Research and Applications, J. Climate, 24, doi: 10.1175/JCLI-D-11-00015.1.

974

975   Schoeberl, M. R., et al. (2007), A trajectory-based estimate of the tropospheric ozone

976   column using the residual method, J. Geophys. Res., 112, D24S49,

977   doi:10.1029/2007JD008773.

978   Semane, N., Peuch, V.-H., El Amraoui, L., Bencherif, H., Massart, S., Cariolle, D., Attié,

979   J.-L. and Abida, R. (2007), An observed and analysed stratospheric ozone intrusion over

980   the high Canadian Arctic UTLS region during the summer of 2003. Q.J.R. Meteorol.

981   Soc., 133: 171–178. doi: 10.1002/qj.141.

982

983   Smit, H. G. J., et al. (2007), Assessment of the performance of ECC-ozonesondes under

984   quasi-flight conditions in the environmental simulation chamber: Insights from the

985   Juelich Ozone Sonde Intercomparison Experiment (JOSIE), J. Geophys. Res., 112,

986   D19306, doi:10.1029/2006JD007308.

987

988   Shindell, D., et al. (2013): Attribution of historical ozone forcing to anthropogenic

989   emissions. Nature Clim. Change, doi:10.1038/nclimate1835

990

991   Stajner, I., et al. (2008), Assimilated ozone from EOS-Aura: Evaluation of the tropopause

992   region and tropospheric columns, J. Geophys. Res., 113, D16S32, doi:10.1029/2007JD008863.

994

995   Steinbrecht, W., H. Claude, U. Köhler, and K. P. Hoinka (1998), Correlations between

996   tropopause height and total ozone: Implications for long-term changes, J. Geophys. Res.,

997   103(D15), 19183–19192, doi:10.1029/98JD01929.

998

999   Strahan, S. E., Duncan, B. N., and Hoor, P. (2007) Observationally derived transport

1000   diagnostics for the lowermost stratosphere and their application to the GMI chemistry and

1001   transport model, Atmos. Chem. Phys., 7, 2435-2445, doi:10.5194/acp-7-2435-2007.

1002

1003   Thompson, A. M., et al. (2003), Southern Hemisphere Additional Ozonesondes

1004   (SHADOZ) 1998–2000 tropical ozone climatology 1. Comparison with Total Ozone

1005   Mapping Spectrometer (TOMS) and ground-based measurements, J. Geophys. Res., 108,

1006   8238, doi:10.1029/2001JD000967, D2.

1007

1008   Waters, J. W. and Co-authors (2006). The Earth Observing System Microwave Limb

1009   Sounder (EOS MLS) on the Aura satellite. *IEEE Trans. Geosci. Remote Sens.*, **44**, 1075–

1010   1092.

1011   Wargan, K., S. Pawson, I. Stajner, and V. Thouret (2010), Spatial structure of assimilated

1012   ozone in the upper troposphere and lower stratosphere, J. Geophys. Res., 115, D24316,

1013   doi:10.1029/2010JD013941.

1014   Worden, H. M., K. W. Bowman, S. S. Kulawik, and A. M. Aghedo (2011), Sensitivity of

1015   outgoing longwave radiative flux to the global vertical distribution of ozone characterized

1016   by instantaneous radiative kernels from Aura-TES, J. Geophys. Res., 116, D14115,

1017   doi:10.1029/2010JD015101.

1018

1019   Wright, J. S. and Fueglistaler, S.: Large differences in reanalyses of diabatic heating in

1020   the tropical upper troposphere and lower stratosphere (2013). Atmos. Chem. Phys., 13,

1021   9565-9576, doi:10.5194/acp-13-9565-2013.

1022

1023   Wu, W.-S., R. J. Purser, and D. F. Parrish (2002), Three-dimensional variational analysis

1024   with spatially inhomogeneous covariances, Mon. Wea. Rev., 130, 2905-2916.

1025   Ziemke, J. R., S. Chandra, G. J. Labow, P. K. Bhartia, L. Froidevaux, and J. C. Witte

1026   (2011), A global climatology of tropospheric and stratospheric ozone derived from Aura

1027   OMI and MLS measurements, Atmos. Chem. Phys., 11, 9237–9251, doi:10.5194/acp-11-

1028   9237-2011.

1029   Ziemke, J. R., et al. (2014), Assessment and applications of NASA ozone data products

1030   derived from Aura OMI/MLS satellite measurements in context of the GMI chemical

1031   transport model, J. Geophys. Res. Atmos., 119, doi:10.1002/2013JD020914.

1032

1033

1034

1035

1036 **Table 1. Mean MLS minus ozonesondes differences averaged over four latitude**

1037 **bands in 2010 at the lowest two levels used in this study[a]**

	60°N-90°N	30°N-60°N	30°S-30°N	South of 30°S
216 hPa	0.05 ppmv	0.06 ppmv	0.02 ppmv	0.03 ppmv
	21%	46%	33%	38%
215 hPa	0.02 ppmv	0.04 ppmv	0.01 ppmv	0.01 ppmv
	5%	17%	17%	8%

1038 [a] The values are expressed in parts per million by volume and as percentage of the sonde

1039 mean.

1040 **Table 2. Statistical description of the sonde-minus-analysis of the LS ozone column**

1041 **separated into latitude bands[a]**

	Bias [DU] (analysis - sondes)	Standard Deviation [DU]	Relative bias [%]	Correlation	Slope	Number of sondes
All sondes	0.50	8.63	0.54	0.99	0.94	18,377
60°N-90°N	-2.08	12.30	-1.75	0.97	0.87	2,548
30°N-60°N	0.43	8.54	0.42	0.98	0.91	9,784
30°S-30°N	1.94	2.77	8.85	0.97	0.92	3,736

1042 [a]All available sondes between 2005 and 2012 were used.

1043

1044

1045

1046

1047

1048

1049

1050

1051

1052

1053

1054

1055 **Table 3. Statistical description of the sonde-minus-analysis of the UT ozone column**

1056 **separated into latitude bands[a]**

	Bias [DU]	Standard Deviation [DU]	Relative bias [%]	Correlation	Slope	Number of sondes
All sondes	1.16	2.82	9.26	0.87	0.71	18,588
60°N-90°N	0.88	1.70	9.88	0.88	0.79	2,553
30°N-60°N	1.02	2.59	7,87	0.85	0.78	9,892
30°S-30°N	2.45	3.83	14.30	0.75	0.44	3,834

1057 [a]All available sondes between 2005 and 2012 were used. Note that the number of sondes

1058 here is greater than in Table 2. This is because there is a small number of soundings that

1059 do not reach the 50 hPa pressure surface but that do reach the tropopause.

1060

1061

1062

1063 **Table 4. Statistical description of the sonde-minus-analysis of the UT ozone column**

1064 **separated into four seasons.**

	Bias [DU]	Standard Deviation [DU]	Relative Bias [%]	Correlation	Slope
DJF	0.72	2.24	7.05	0.87	0.73
MAM	0.98	2.66	7.9	0.86	0.75
JJA	1.42	3.41	9.28	0.81	0.60
SON	1.54	2.59	12.90	0.88	0.69

1065

1066

1067

1068

1069

1070 **Table 5. Distributions and physical descriptions of the low-ozone laminae**

1071 **determined from HIRDLS retrievals and from the GEOS-5 MLS+OMI analyses[a]**

	HIRDLS, February	Analysis, February	HIRDLS, April	Analysis, April
Thickness (mean [K])	42.83	42.40	43.82	44.93
Thickness (standard deviation [K])	9.98	8.70	9.44	8.88
Magnitude (mean [%])	27.15	25.66	31.40	30.32
Magnitude (standard deviation [%])	11.86	11.69	12.12	11.45
Count	590	386	1131	807

1072 [a] Results are shown for February and April, corresponding to the plots shown in Figure

1073 14.

1074

1075

1076

1077

1078
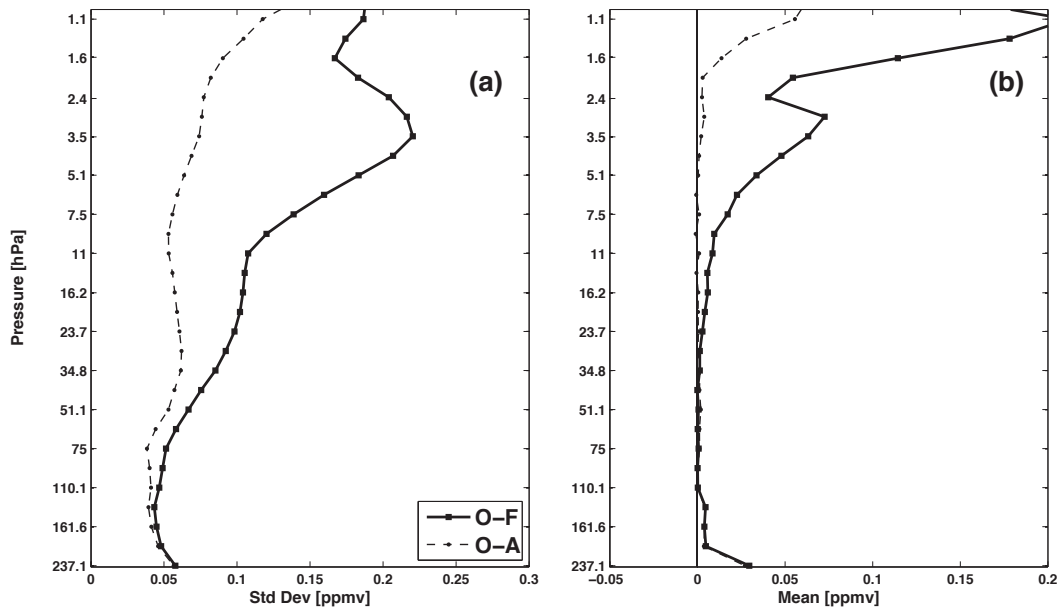
1079

Figure 1. Altitudinal profiles of (a) the standard deviations and (b) the means of the O-F and O-A residuals for Microwave Limb Sounder (MLS) ozone mixing ratios, for June, July and August 2010, in the 30°N-90°N latitude band. Units are part per million by volume (ppmv).

1080

1081

1082

1083

1084

1085
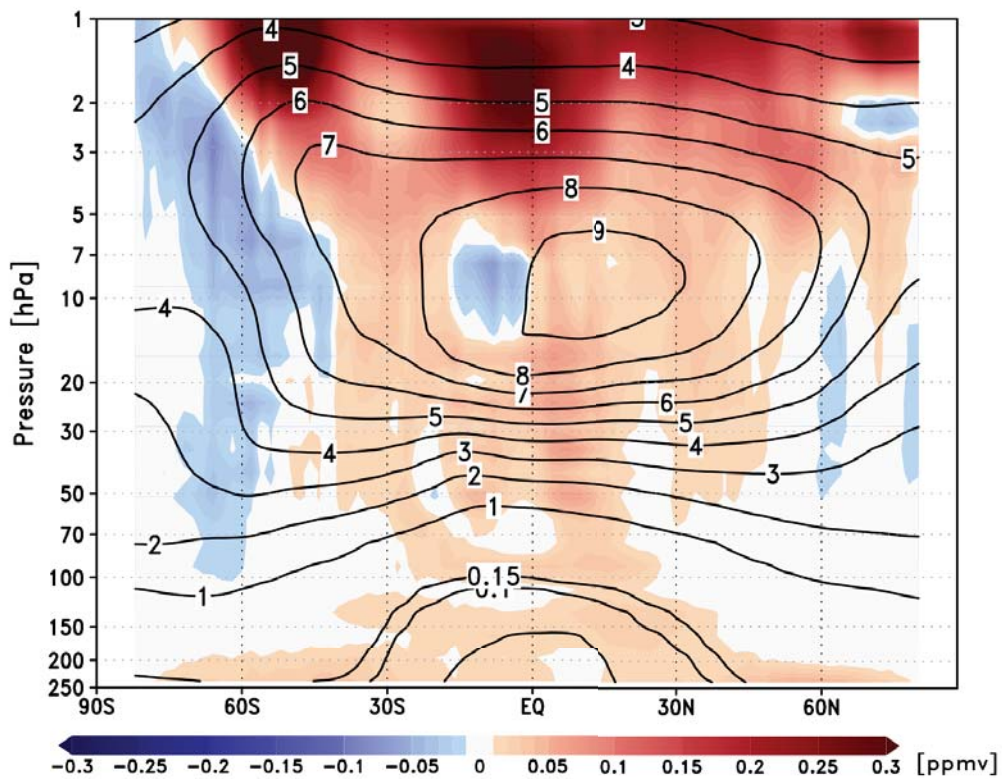
1086

Figure 2. Zonal mean MLS O-Fs in June – August 2010 (shaded) and the mean

background ozone from 6-hourly forecasts (contours).

1089
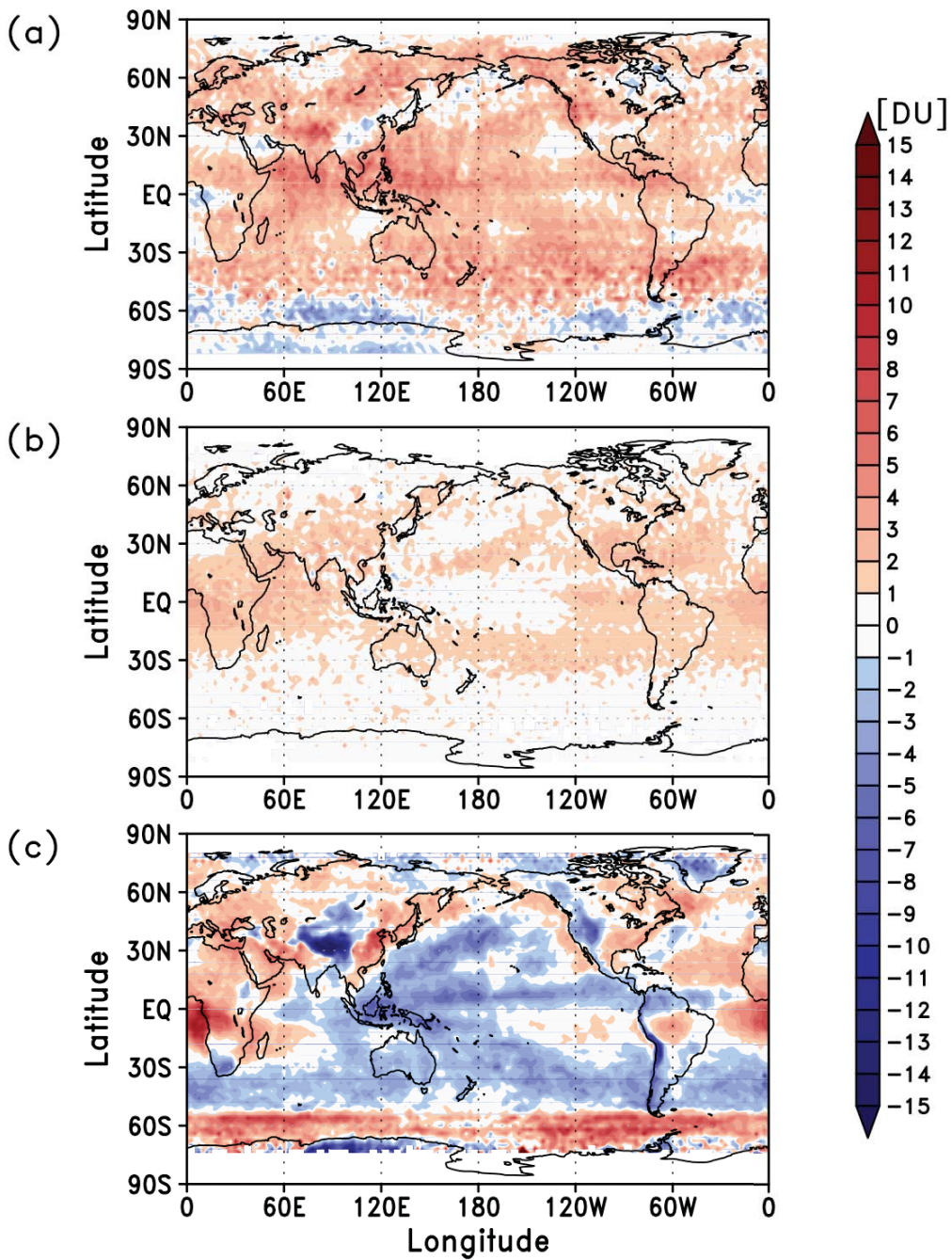
Figure 3. The spatial distribution of the mean O-F residuals for partial ozone

columns, averaged over June-July –August (JJA) 2010.   (a) The stratospheric

1093   **portion of the MLS profile, obtained by integrating MLS O-F profiles between the**

1094   **tropopause and 0.01hPa. (b) For the upper tropospheric portion of the MLS profile**

1095   **measurements, integrated between 237 hPa and the tropopause. (c) For the Ozone**

1096   **Monitoring Instrument (OMI), weighted by the column-specific efficiency factors**

1097   **(according to Eq. 1). In (a, b) the tropopause is defined as the 100 hPa surface**

1098   **between 10°S – 10°N and the 2 PVU surface elsewhere.**
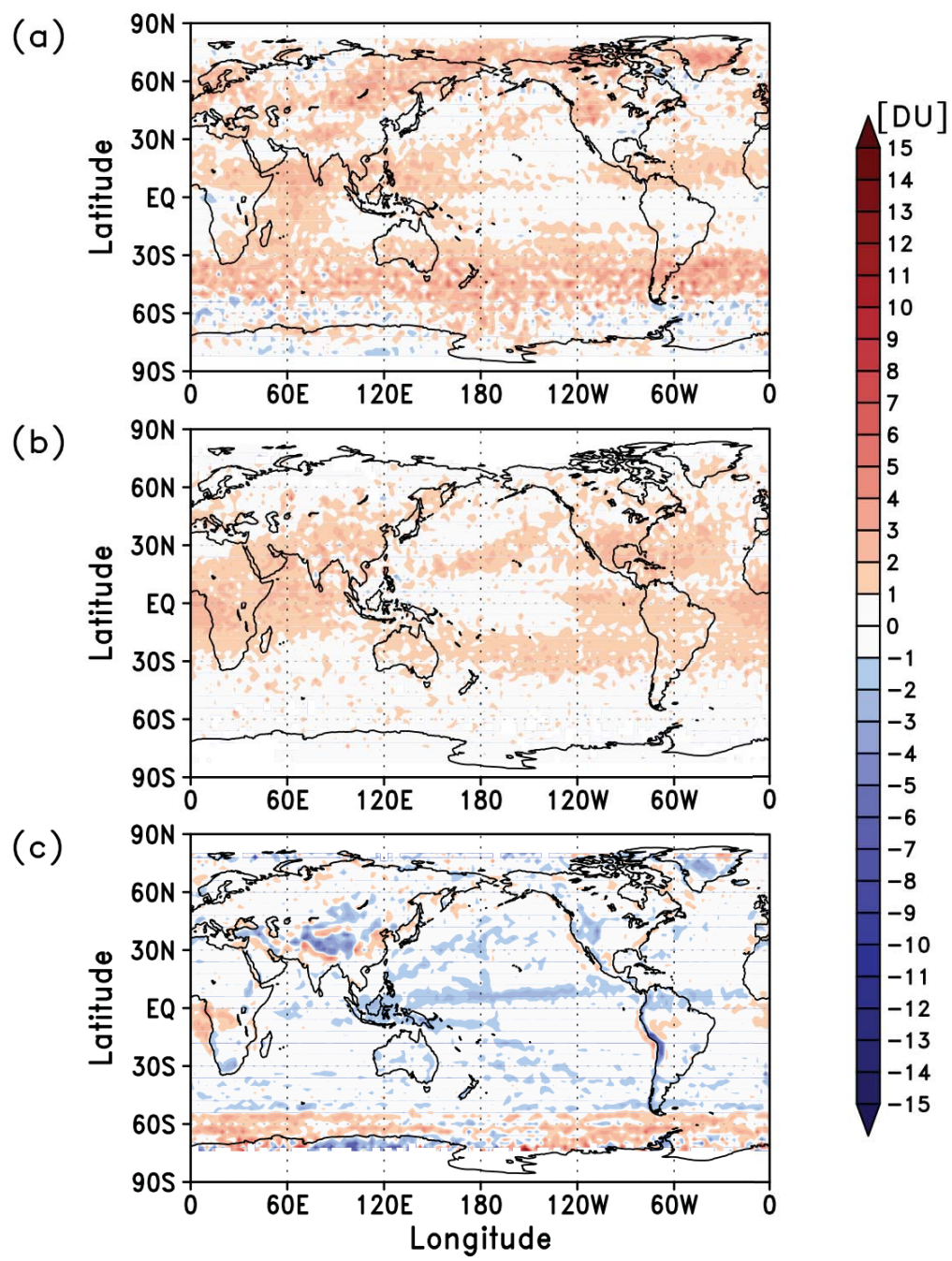
1099

Figure 4. As in Figure 3B, but for the observation-minus-analysis (O-A) fields.

1101
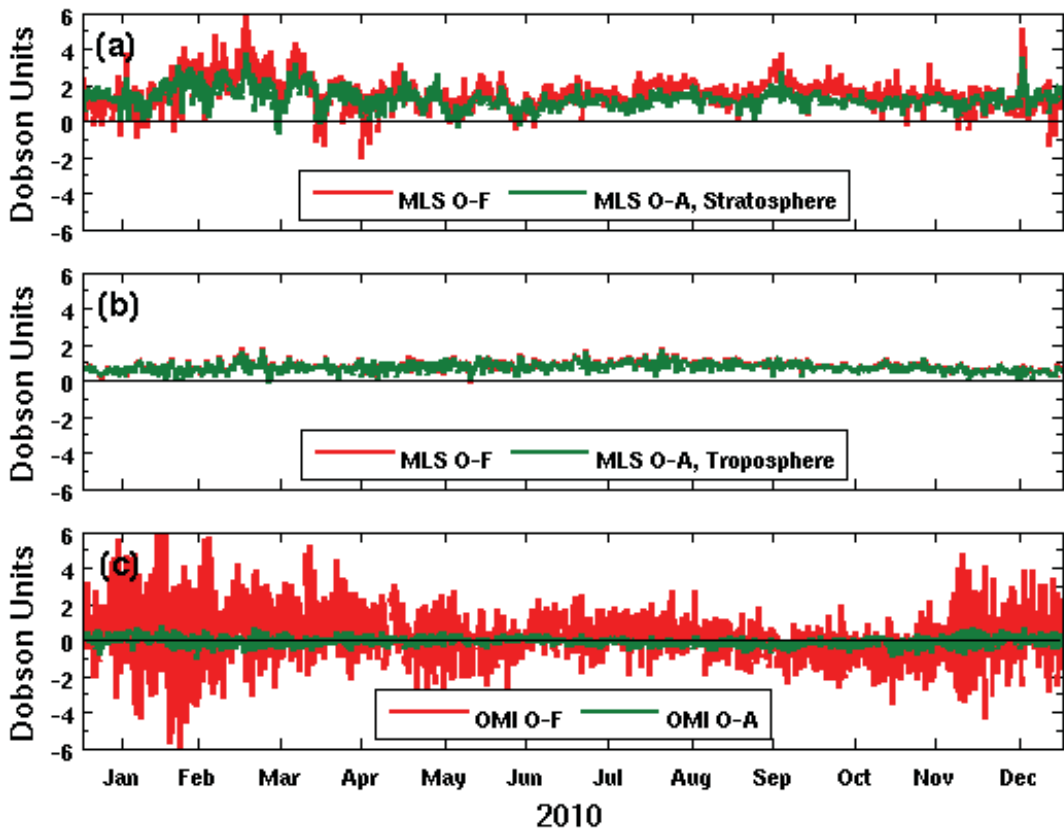
Figure 5. Time series of the global-mean, six-hourly O-F (red) and O-A (green) statistics (DU) from the ozone analysis. Data are shown for (a) the MLS stratospheric column; (b) the MLS upper tropospheric column; and (c) the OMI weighted column. These three panels show time series for the same three layers as annual mean maps shown in Figures 3 and 4.

1112
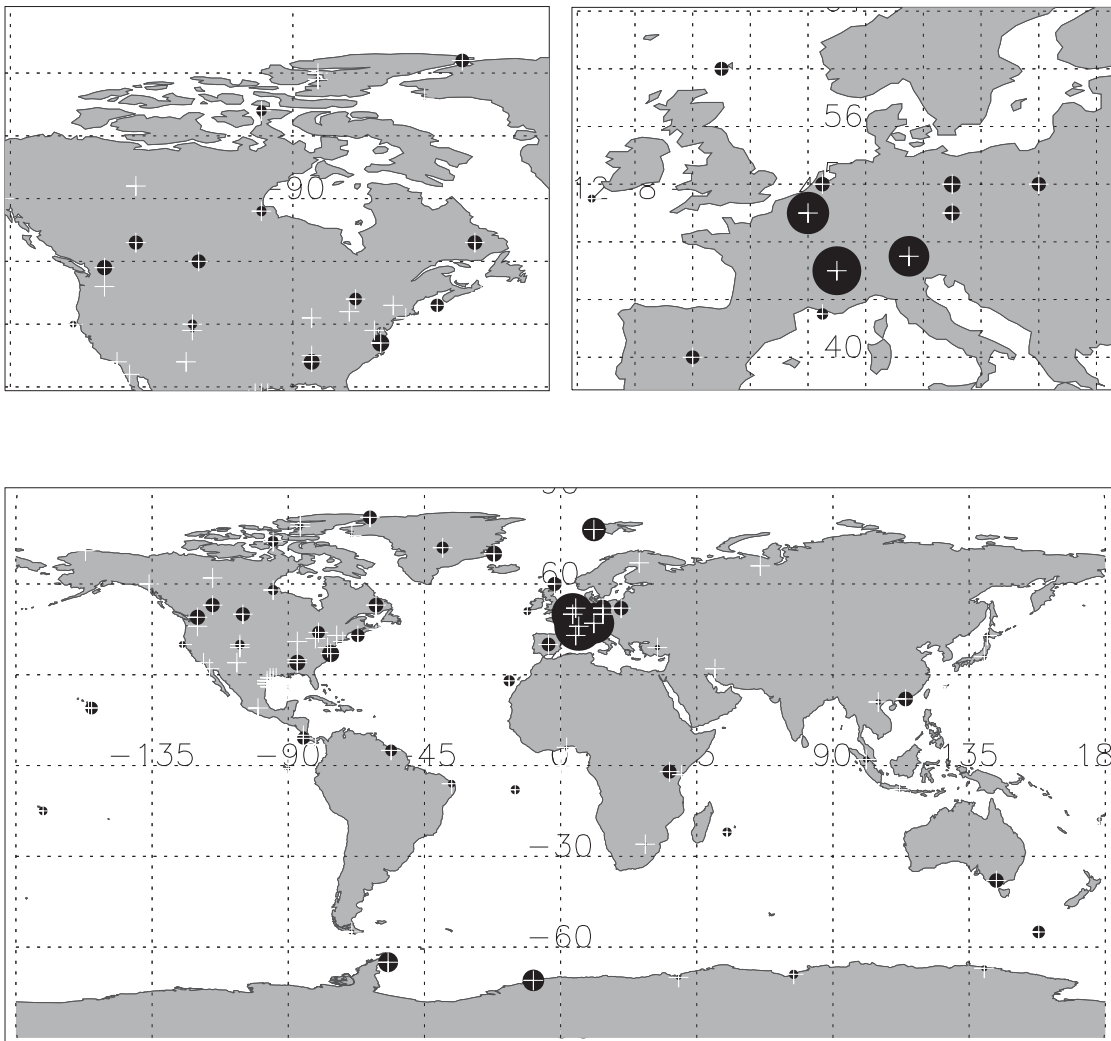
Figure 6. Locations of the ECC ozone sondes for the years 2005 - 2012 used in this study, shown separately for North America, Europe, and the globe. Each station is marked by a white plus sign and a filled black circle scaled by the number of soundings at that location.

1117
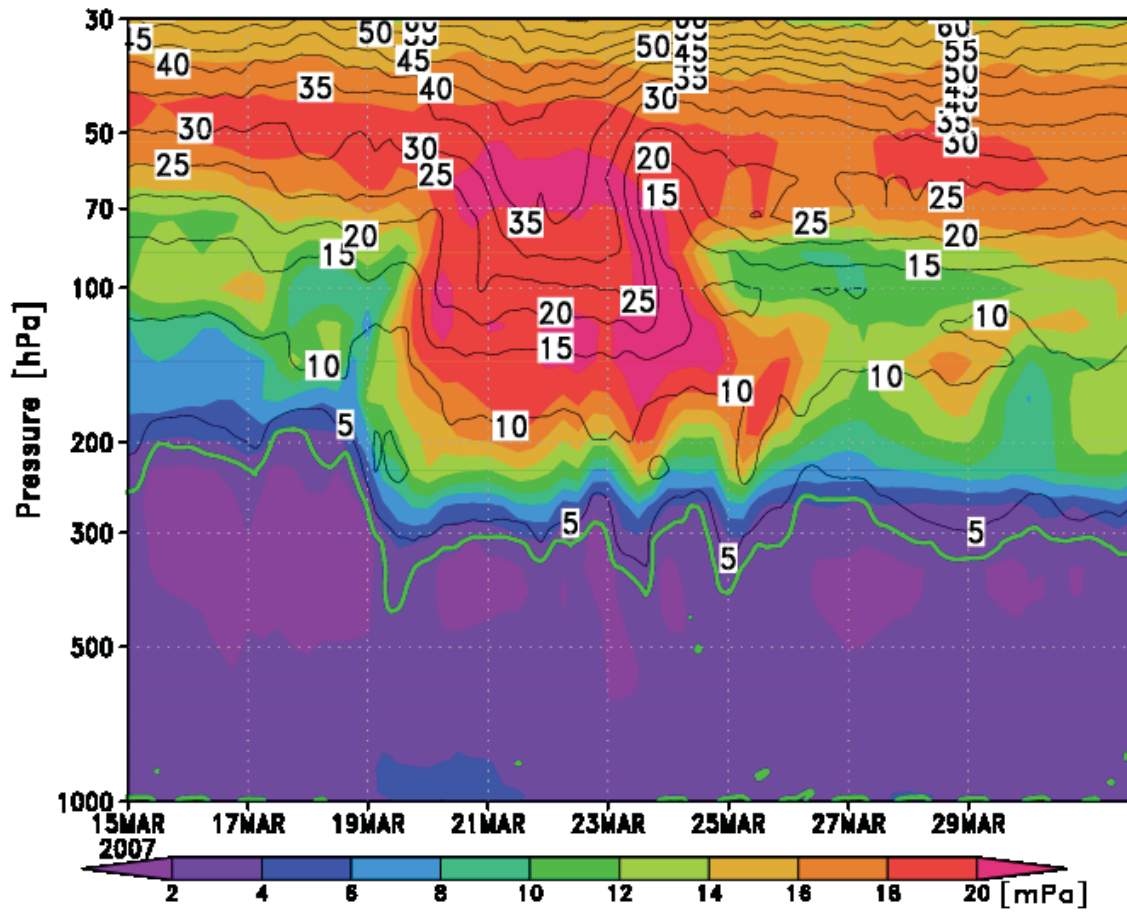
Figure 7. Evolution of analyses of ozone partial pressure (shaded) and potential vorticity (contours) at the GEOS-5 grid location above Hohenpeissenberg between March 15 and March 31 2007. Values are available every six hours. The 2 PVU line, which defines the tropopause in this study, is shown in green.
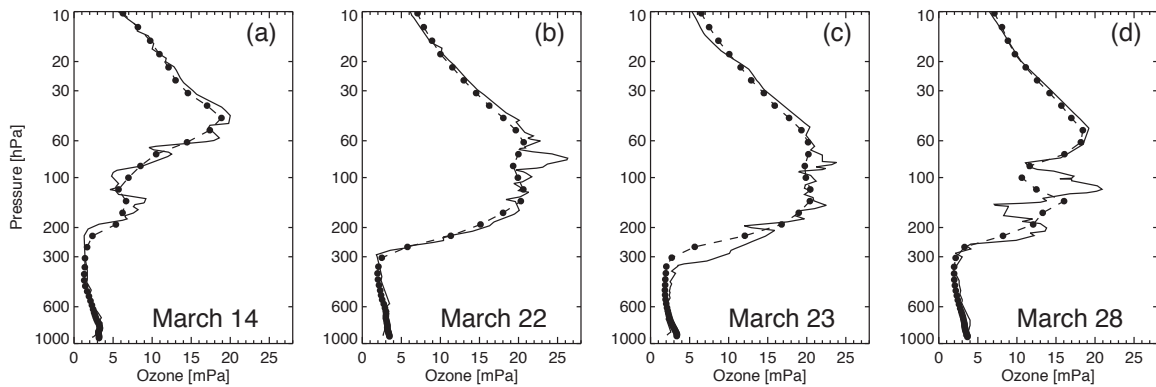
1125

1126 **Figure 8. Ozone profiles from Hohenpeissenberg sondes (solid) and the GEOS-5**

1127 **analyses (dashed) on March 14 (a), 22 (b), 23 (c), and 28 (d), 2007. The GEOS-5**

1128 **values are shown on the vertical grid of the model, indicated by the solid black dots.**

1129

1130
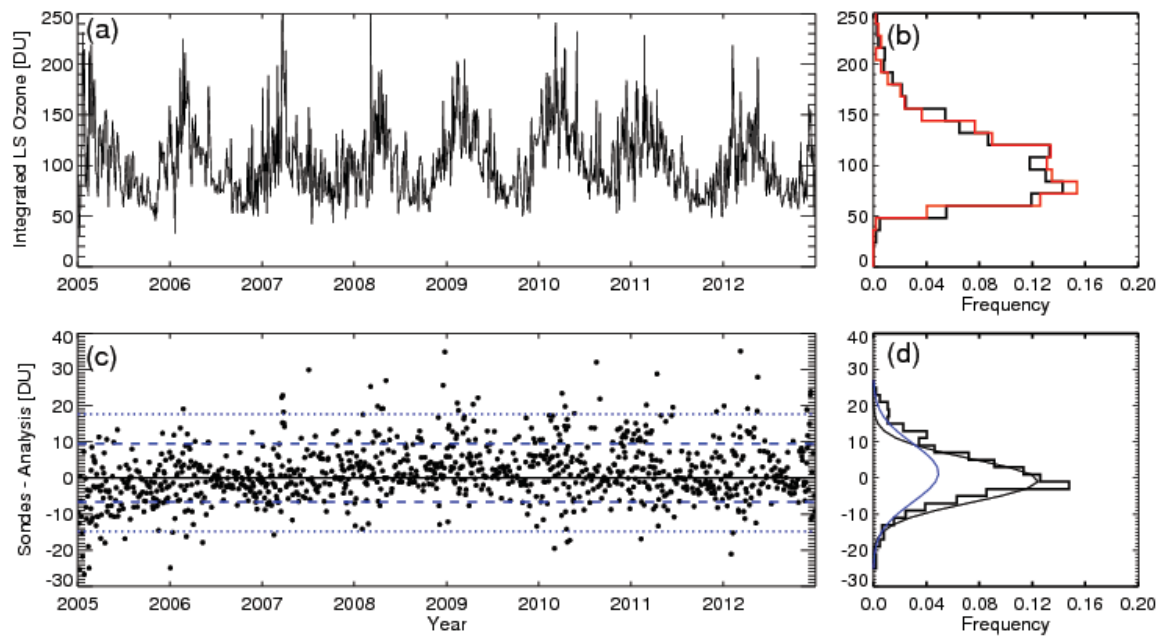
1131

1132   **Figure 9. A comparison of lower stratospheric (LS) ozone partial columns in milli-**

1133   **atmospheric centimeters (Dobson Units, DU) at Hohenpeissenberg (47°48'N, 11°E).**

1134   **Analyses from GEOS-5 were sampled at the times of 1016 in-situ sonde observations**

1135   **made between 2005 and 2012. (a) Time series from the sondes. (b) The probability**

1136   **distribution function (p.d.f.) computed for the sonde observation (black) and the**

1137   **GEOS-5 analysis (red). (c) Time series of the sonde-minus-analysis differences**

1138   **together with the 1-σ and 2-σ intervals (the blue dashed and dotted lines,**

1139   **respectively). (d) the p.d.f. of the sonde-analysis differences (stepped), a Gaussian fit**

1140   **to this distribution (smooth black curve), and the Gaussian probability density**

1141   **function with the mean and standard deviation as computed from the sonde –**

1142   **analysis differences (blue) . The bin sizes used to compute the distributions in**

1143   **panels (b) and (d) are 12 DU and 2 DU, respectively.**
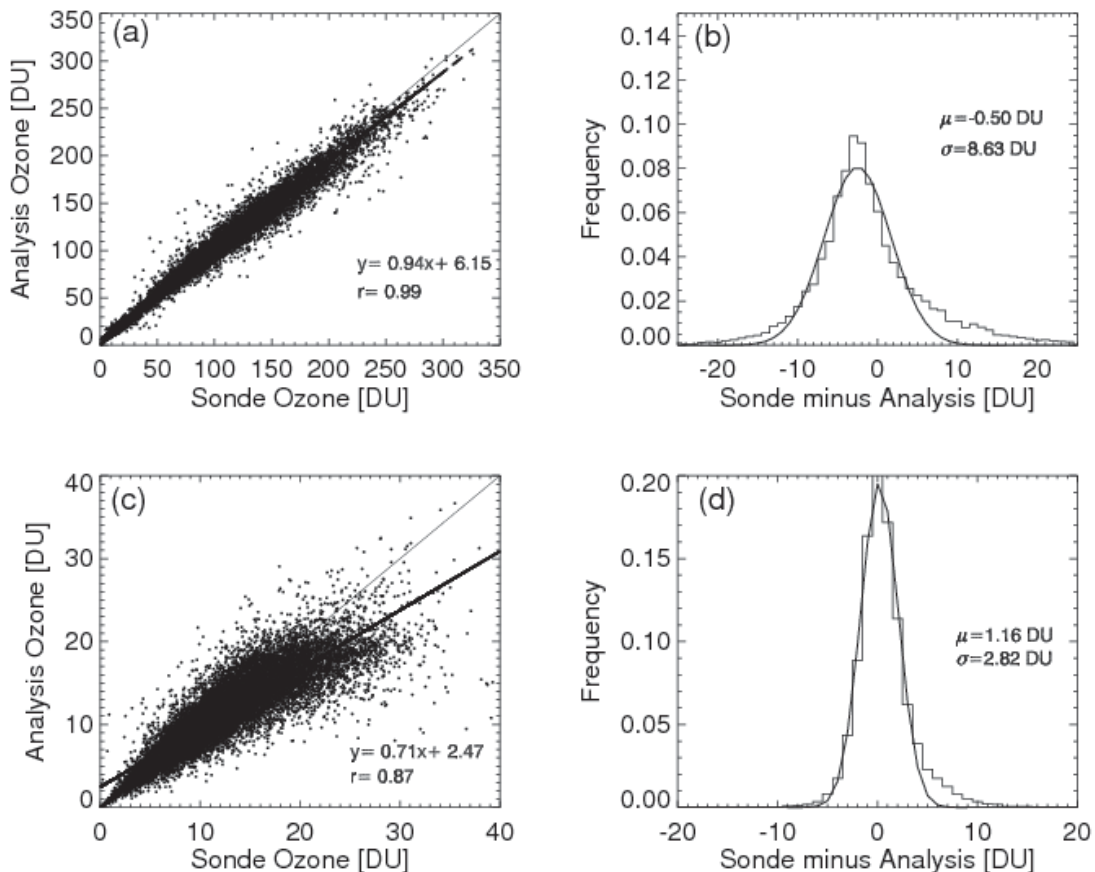
1144

Figure 10. Comparisons of the analyzed UTLS ozone with the collocated ozonesonde observations. (a) Scatter plot of the lower stratospheric partial column, integrated between the tropopause and 50hPa. The thick black line represents a linear fit to the data plotted. (b) The binned distribution of the sonde-minus-analysis differences (stepped line) along with a Gaussian fit to this distribution (smooth curve). Panels (c) and (d) show the equivalent plots for the upper tropospheric layer (500 hPa to the tropopause). This comparison includes about 16,000 sonde observations, with no sorting by their spatial or seasonal locations.

1145

1146

1147

1148

1149

1150

1151

1152

1153
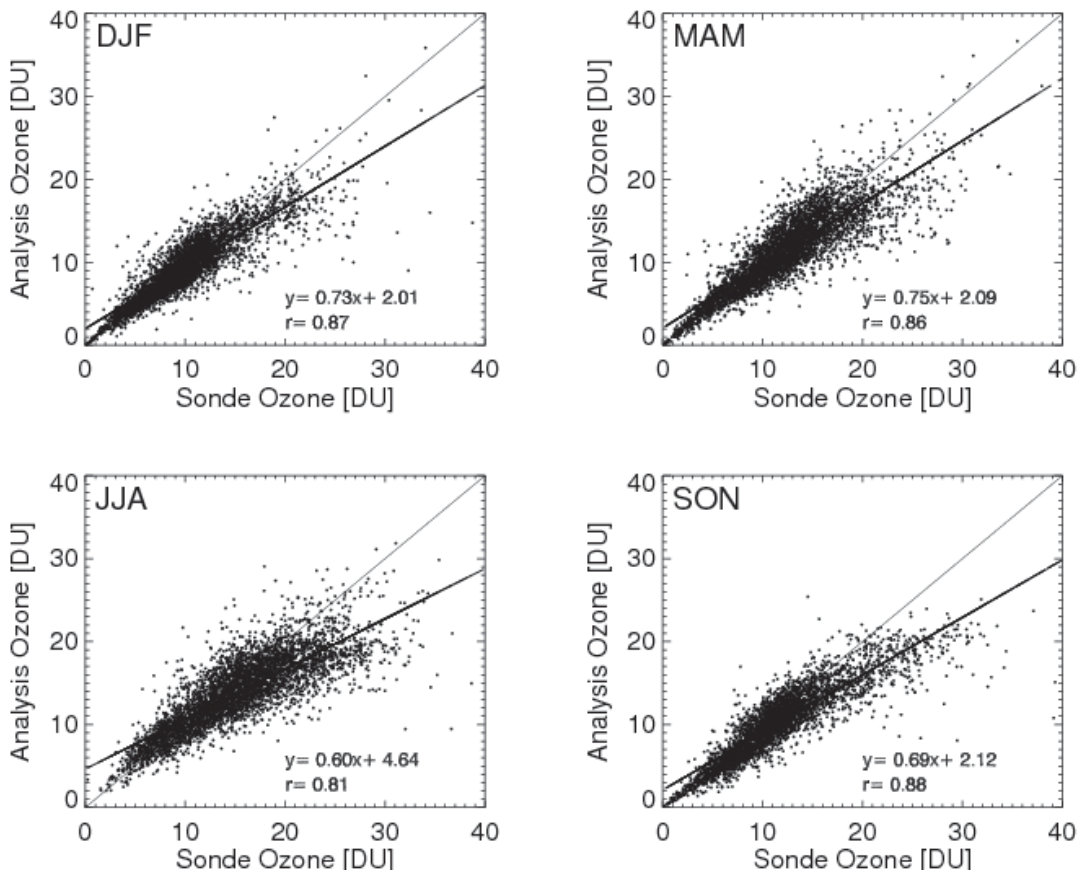
1154

Figure 11. Scatter plots of partial UT ozone columns in sondes (ordinates) and the

GEOS-5 analyses (abcissae) for showing the relationship between sonde and

analysis ozone in the upper troposphere, computed from all available sondes

between 2005 and 2012 and separated by season. (a) December – January –

February (DJF), (b) March – April – May (MAM), (c) June – July – August (JJA),

(d) September – October – November (SON).

1161

1162

1163
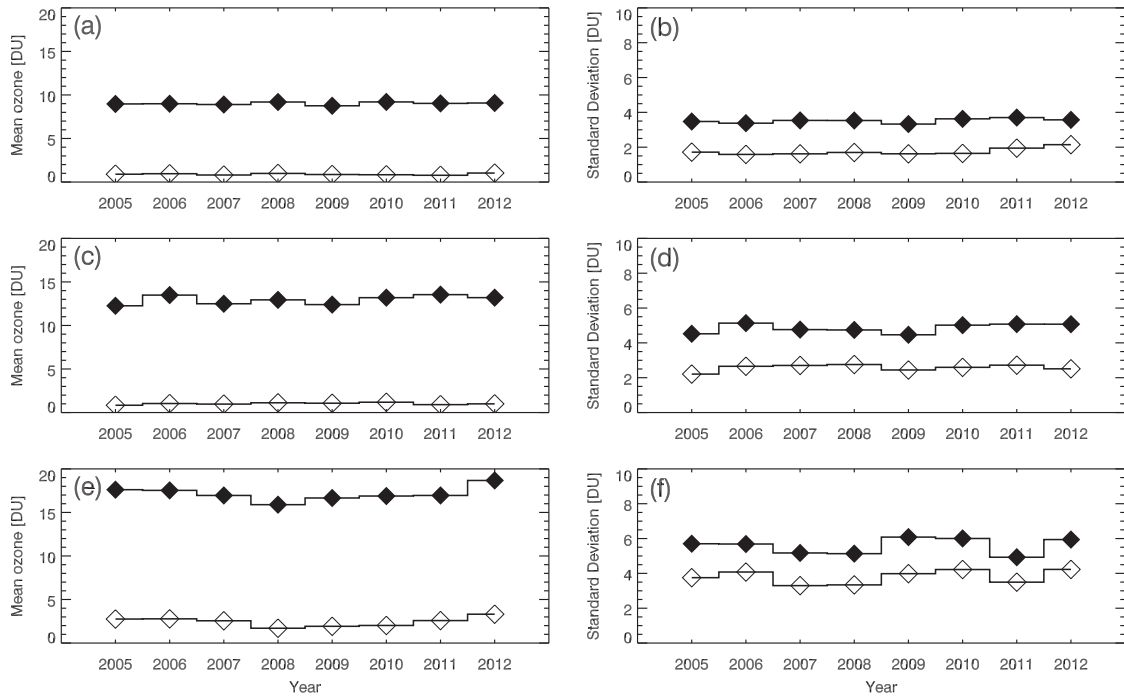
1164

Figure 12. Time series of annual-mean UT sonde ozone statistics. (left column: panels a, c, e) The mean partial columns (DU: black diamonds) and the mean sonde-minus-analysis differences (open diamonds) and (right column: panels b, d, f) standard deviations of the same quantities. Results are shown for (top row: panels a, b) 60°N-90°N, (middle row: panels c, d) 30°N-60°N, and (bottom row: panels e, f) 30°S-30°N.
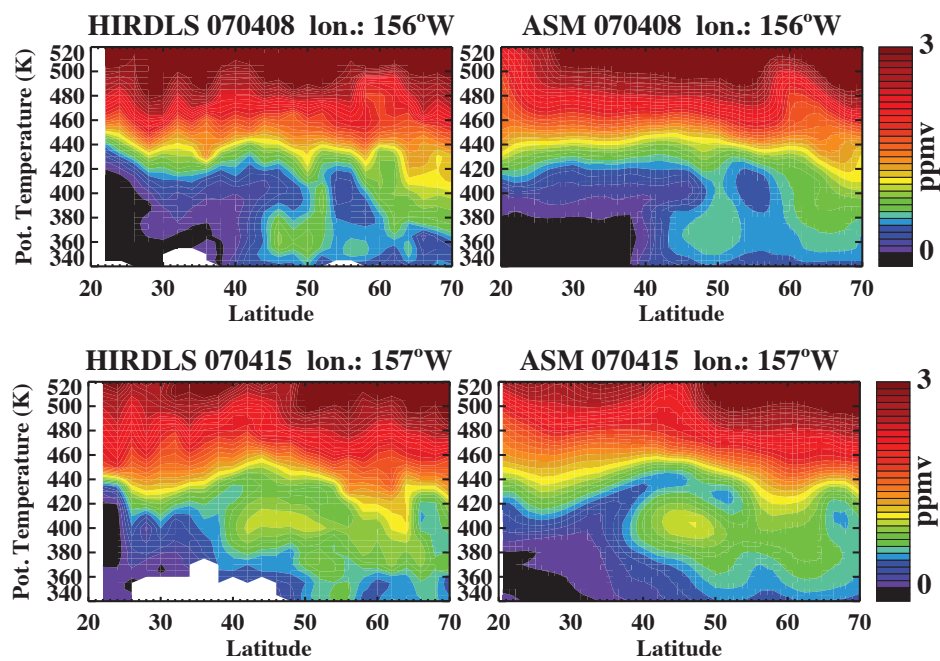
Figure 13. Cross-sections of the UTLS ozone as a function of latitude and potential temperature from HIRDLS (left) and the analysis (right) at 156°W on April 8th 2007 (top) and 157°W on April 15th 2007 (bottom)

1184
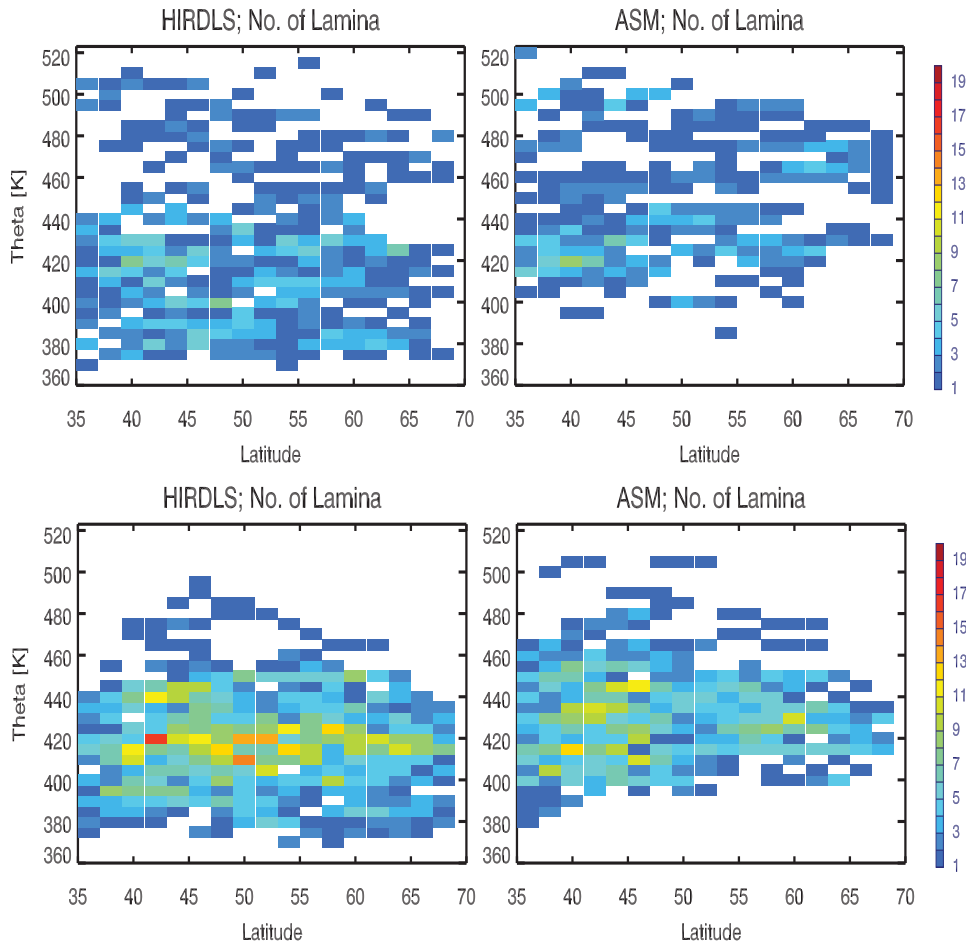
Figure 14. Zonally summed counts of low ozone laminae from HIRDLS (left) and the assimilation (right) in February (top) and April (bottom) 2007. The vertical coordinate is potential temperature.

1188

1189

1190
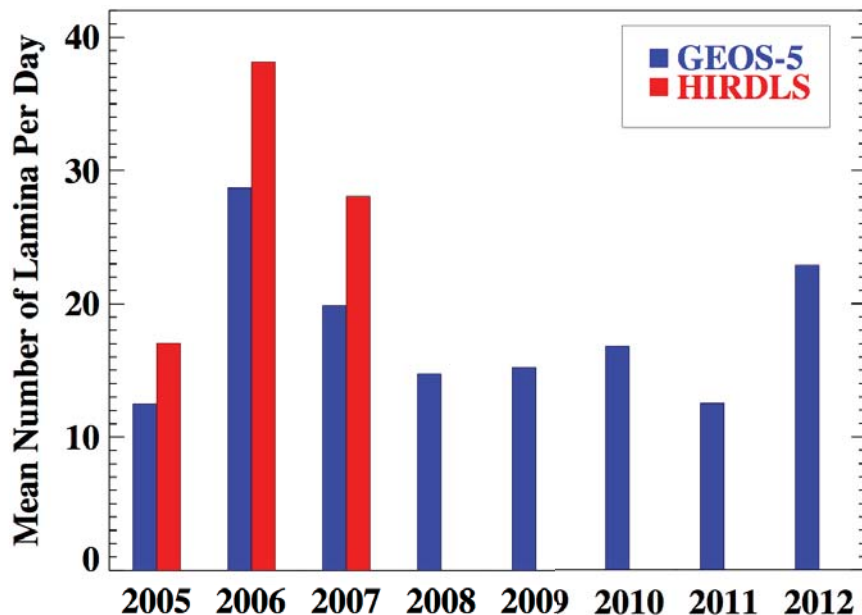
1191

1192 **Figure 15. Mean number of laminae identified per day in February-May for each**

1193 **year in the NH mid-latitudes between 340 K and 550 K potential**

1194 **temperature. Results from GEOS-5 analysis (blue) are compared to the three years**

1195 **of available HIRDLS observations (red).**